

Blood Flow Disturbances Downstream of an Endovascular Stent-Graft: An
Experimental Investigation of Oversizing and Compliance Mismatch

by

Amanda Colella-Centazzo

Submitted in partial fulfilment of the requirements
for the degree of Master of Applied Science

at

Dalhousie University
Halifax, Nova Scotia
October 2015

© Copyright by Amanda Colella-Centazzo, 2015

Table of Contents

List of Tables.....	v
List of Figures.....	vi
Abstract.....	x
List of Abbreviations and Symbols Used	xi
Acknowledgements.....	xii
Chapter 1 - Introduction	0
1.1 Background & Motivation.....	0
1.2 Objectives	2
1.3 Summary.....	3
Chapter 2 – Background & Literature Review: Stent Performance and Limitations.....	4
2.1 Introduction	4
2.2 Overview of Stent Structure and Design.....	4
2.3 Hemodynamics and Stent Patency.....	8
2.3.1 Introduction.....	8
2.3.2 Physiological Environment	9
2.3.3 Vascular Remodeling and Intimal Hyperplasia.....	12
2.3.4 Atherosclerotic Plaques & Thrombus Formation.....	14
2.4 Compliance Mismatch.....	15
2.5 Stent Induced Blood Flow Disturbances	18
2.6 Conclusion.....	22

Chapter 3 – Methodology: PIV Experimental Set-up and Image Acquisition	24
3.1 Introduction	24
3.2 Experimental Set-up Overview.....	24
3.3 Blood Analog Fluid and Flow Properties.....	27
3.4 Mock Arteries.....	30
3.5 Image Acquisition and Processing.....	36
3.6 Data Processing.....	38
Chapter 4 – Results.....	40
4.1 Introduction	40
4.2 PIV Validation and Calibration.....	40
4.2.1 Steady Flow of Water in Acrylic	40
4.2.2 Steady Flow of Non-Newtonian Analog in Silicone.....	41
4.2.3 Non-Newtonian Analog under Pulsatile Flow	42
4.2.4 Pulsatile Flow in Elastic Tubes	44
4.3 Acrylic Tubes.....	48
4.3.1 Individual Stent Wires.....	48
4.3.2 Full Stents	50
4.4 Healthy Compliant Vessel.....	54
4.4.1 – Individual Stent Wires.....	54
4.4.2 – Full Stent.....	57
4.5 Variable Vessel Compliance	60

Chapter 5 –Discussion	65
5.1 Implications.....	65
5.1.1 Individual Wires	65
5.1.2 Effect of Stent Cover	66
5.1.3 Effect of Oversizing and Compliance Mismatch.....	67
5.2 Limitations.....	69
Chapter 6 – Conclusions and Recommendations	71
6.1 Summary and Conclusion.....	71
6.3 Future Work and Recommendations.....	72
References.....	74
Appendix A- Results Matlab Code.....	82
Appendix B- Pump Settings.....	86

List of Tables

Table 3-1 - Measured compliance of mock arteries of varying base to curing agent ratios	35
Table 3-2 Inner diameter at stent exit after implantation of a 12 mm and 14 mm stent- graft for 3 compliances of elastic arteries at zero flow.	37
Table 4-1 - Axial flowrates and volume stored at peak pulse for a range of test section elasticities under pulsatile flow conditions using a non-Newtonian blood analog. ...	45
Table 4-2 - Cycle averaged WSS and OSI for three compliant and one rigid tube using a non-Newtonian blood analog under pulsatile flow conditions.	47

List of Figures

Figure 1-1 – Stent-grafts are used to re-establish a healthy luminal diameter and redirect blood flow across the aneurysmal bulge.....	1
Figure 2-1 - 12mm Cook Zenith Gianturco Stent-Graft.	7
Figure 2-2 - A segment of an artery showing the endothelial monolayer and the forces that act on it, namely the WSS (τ) and the radial pressure (p) [17].	10
Figure 2-3 - Effect of fluid flow on morphology and alignment of endothelial cells [9]. ..	11
Figure 2-4 - Illustration taken from Edelman & Rogers [19] showing the phases of vascular repair which are the crucial mechanisms associated with a narrowing luminal diameter in the weeks after stenting. SAM and TIM refer to surface-adherent monocytes and tissue-infiltrating monocytes, respectively.....	12
Figure 3-1 - Schematic representation of experimental flow loop simulating arterial blood flow and PIV image acquisition system.....	25
Figure 3-2 – View of experimental PIV set-up constructed for image acquisition of flow through test chamber. Arrows indicate direction of flow.....	26
Figure 3-3 – Three 12 mm stent wires removed from their polyester cover and deployed inside a 10 mm inner diameter compliant mock artery.	27
Figure 3-4 – Viscosity calculations across a range of strain rates for the Glycerol-Water-Xanthan mixture measured using a pressure drop pipe set-up.	29
Figure 3-5 – a) Typical 1 Hz flow profile in the femoral artery adapted from Ku [46]; b) Velocity profiles across pulse cycle recorded by PIV.....	30
Figure 3-6 – Three part machined steel molds used to manufacture silicone mock arteries.	32
Figure 3-7 - Sylgard vessel affixed in acrylic test section.....	33

Figure 3-8 – a) PIV image acquired using Photron Mini UX100 of a Sylgard® tube at the exit of a single stent wire. Yellow dashed lines indicated the selected ROI; b) Vector field output for a single frame sequence.36

Figure 3-9 - PIV image of a 12 mm stent implanted within a silicone mock artery at resting flow, illustrating the expansion in luminal diameter and tapering downstream of the stent.37

Figure 4-1 - PIV measured velocity profile in non-stented steady flow through a rigid acrylic test section compared to the Poiseuillian flow estimation. Error bars represent standard deviations of velocity measurements.....41

Figure 4-2 - PIV measured velocity profile in non-stented steady flow through a rigid acrylic test section and a compliant mock artery (C_{Base}) at a flow rate of 354 ml/min using a blood analog. Error bars represent standard deviations of velocity measurements.....42

Figure 4-3 - Flowrates calculated based on instantaneous piston velocities compared to those obtained from PIV data.....43

Figure 4-4 – Pulse flow rates averaged over 10 pulses in acrylic tube for all stent configurations. Error bars represent standard deviations of flow measurements in mL/s for the six test configurations.44

Figure 4-5 – Peak velocity profiles measured in rigid acrylic tube and compliant Sylgard® mock artery with no stent. Error bars represent normalized standard deviations. All velocities are normalized using maximum velocity in the acrylic tube.46

Figure 4-6 –PIV velocity measurements (normalized using the maximum velocity of the no stent case) from near-wall to tube center measured at $x/R = 0.5$ from outlet of a single stent wire compared to non-stented flow in a rigid acrylic tube.....48

Figure 4-7 - Normalized WSS in single wire stented flow across pulse cycle at $x/R = 0.5$ from stent outlet compared to non-stented flow.....49

Figure 4-8 - PIV velocity measurements (Normalized using maximum velocity of no stent case) from near-wall to tube center measured at $x/R = 0.5$ from outlet of a three stent wire configurations in a rigid acrylic tube. Error bars represent normalized standard deviations.49

Figure 4-9 - Normalized PIV velocity measurements across entire diameter measured at $x/R = 0.5$ from stent outlet for a 12 mm and 14 mm full stent at peak pulse in a rigid acrylic tube. Error bars represent normalized standard deviations.51

Figure 4-10 - Velocity contour plots from $x/R = 0.5$ to $x/R = 3.0$ for Non-stented flow (A). downstream of a 12 mm (B) and 14 mm (C) stent.....51

Figure 4-11 - Normalized WSS across the pulse for the 12 mm and 14 mm stent compared to the non-stented flow.....52

Figure 4-12 - Axial turbulence intensities in non-stented flow (A) and downstream of a 12mm (B) and 14mm (C) Gianturco stent at peak pulse in an acrylic tube.53

Figure 4-13- Normalized PIV velocity measurements from wall to tube center measured at $x/R = 0.5$ from outlet of a single stent wire compared to non-stented flow in a compliant mock artery (C_{Base}). Error bars represent normalized standard deviations.55

Figure 4-14 - Normalized WSS in single wire stented flow across pulse cycle at $x/R = 0.5$ from stent outlet compared to non-stented flow.....55

Figure 4-15 - Normalized PIV velocity measurements from wall to tube center measured at $x/R = 0.5$ from outlet of a three stent wire configurations within a compliant mock artery. Error bars represent normalized standard deviations.56

Figure 4-16 - Centerline velocities measured at $x/R=0.5$ from stent exit for one, two, three stent wires. Error bars represent normalized standard deviations.56

Figure 4-17 - Normalized PIV velocity measurements measured at $x/R = 0.5$ from the stent exit in a compliant mock artery across entire diameter. Error bars represent normalized standard deviations.57

Figure 4-18- Normalized PIV velocity measurements from wall to tube center measured at $x/R = 0.5$ from the stent exit in a compliant mock artery (C_{Base}) for both a 14mm and 12 mm stent. Error bars represent normalized standard deviations.58

Figure 4-19 - Normalized WSS across pulse cycle at $x/R = 0.5$ from outlet of a 12 mm and 14 mm stent compared to non-stented flow.....58

Figure 4-20 - Axial turbulence strengths non-stented flow (A) downstream of a 12 mm (B) 14 mm (C) Gianturco stent at peak pulse in a 7.7 % mm Hg- 1×10^{-2} compliant tube.59

Figure 4-21 - Normalized PIV velocity measurements from wall to wall measured at $x/R = 0.5$ from a stent exit in a compliant mock artery. Error bars represent normalized standard deviations.60

Figure 4-22 - Axial turbulence strengths non-stented flow (A) and downstream of a 12mm (B) and 14mm (C) Gianturco stent at peak pulse in a 6.2 % mm Hg- 1×10^{-2} compliant tube.61

Figure 4-23 - Normalized WSS across pulse cycle at $x/R = 0.5$ from outlet of a 12 mm and 14 mm stent compared to non-stented flow.....62

Figure 4-24 - Normalized PIV velocity measurements across tube diameter measured at $x/R = 0.5$ from a stent exit in a compliant mock artery (C_{High}). Error bars represent normalized standard deviations.....63

Figure 4-25 - Normalized PIV velocity measurements shown in Figure 4-24, without error bars.64

Figure 4-26 - Normalized WSS across pulse cycle at $x/R = 0.5$ from outlet of a 12 mm and 14 mm stent compared to non-stented flow.....64

Abstract

In current medical practice, endovascular stents are used in the treatment of arterial disease, particularly to bridge blood flow through aneurysmal vessels. Although this is the preferred treatment for such conditions many secondary issues can arise post-implantation, with the primary concern being endoleak due to improper sealing proximal and distal to the stent. Furthermore, the fluid dynamic forces which are altered upon stent introduction play an important role in tissue healing and by extension stent efficacy. These flow disturbances are exacerbated by a difference in compliance between the stented area and the native vessel. In addition to the implications in tissue behavior, a better understanding of the flow patterns induced by various stents will be valuable when refining and conceiving improved methods for affixing the stent and reducing the occurrence of endoleaks.

An experimental investigation was conducted to better understand the flow disturbances caused by stent introduction. Specifically, this study measures changes in velocity profiles, turbulence intensities, wall shear stress, and the oscillatory shear index, which have all been shown to directly affect endothelial phenotype expression and consequently stent patency. Using particle image velocimetry, flow through Gianturco Z-wire stents was visualized and quantified. The test set-up allows for the stent to be deployed in a 10 mm tube and exposed to pulsatile flow comparable to that of a human peripheral artery. Each experiment is carried out in a rigid acrylic tube, as well as three mock arteries having compliances within the clinically observed range.

Flow disturbances induced by the stents caused an increase in centerline velocities and an accompanying decrease at the vessel periphery, with some reverse flow noted at the wall. Implantation of a single stent wire caused minor disturbances to the flow, however additional wires had no subsequent effect on the flow profiles measured downstream. The introduction of a jacketed stent had a similar, yet more pronounced effect on the flow, causing increases in the centerline velocities between 41-86.2% at peak flow and inducing drops to the velocity at the wall which in turn lowered the wall shear stress.

List of Abbreviations and Symbols Used

AAA – Abdominal Aortic Aneurysm	ΔP – Pressure Change
ABS – Acrylonitrile Butadiene Styrene	r – Local Radius
C – Compliance	R – Total Radius
CMS – Compliance Matching Stents	ROI – Region of Interest
CFD – Computational Fluid Dynamics	n – Refractive Index
D – Diameter	Re – Reynold’s Number
ΔD – Diametrical Change	γ – Shear Strain
DES – Drug Eluding Stents	γ_a – Apparent Shear Strain
Le – Entrance Length	γ_c – Corrected Shear Strain
FOV – Field Of View	τ – Shear Stress
FEM – Finite Element Modeling	SMC – Smooth Muscle Cells
Q – Flow Rate	v_i' – Turbulence Fluctuations
FL – Focal Length	\bar{v} – Average Velocity
ID – Internal Diameter	v_i – Instantaneous Velocity
LDA – Laser Doppler Anemometry	μ – Viscosity
OSI – Oscillatory Shear Index	μ_c – Corrected Viscosity
OD – Outer Diameter	μ_0 – Viscosity at Zero Shear
p – Radial Pressure	μ_∞ – Viscosity at Infinite Shear
λ – Relaxation Constant	WSS – Wall Shear Stress
PIV – Particle Image Velocimetry	x – Distance from Stent Exit
N – Power Index	

Acknowledgements

My sincere thanks to all of the great professors, technicians and collaborators who have deeply contributed to my knowledge and appreciation of their respective expertise—specifically Professor Darrel Doman, Professor Gianfranco Mazzanti, Angus MacPherson and Reginald Peters.

I would like to extend my deep gratitude to my friends and colleagues in my research group for consistently sharing with me their knowledge and skills on such an extensive breadth of subjects. Particularly, Chris Brake, who designed and constructed the heart mimicking pump used in this work.

Furthermore, I would like to acknowledge the work of our diligent research assistants who contributed to the work presented in this thesis, Alyson Petsche and Joe Elsmere, and wish them a future free from Sylgard 184 and its derivatives.

Of course I am enormously thankful for the immeasurable love and support from my parents, Enzo and Patricia, and my two truly wonderful sisters, Sabrina and Isabella, who continue to inspire me with their creativity, ingenuity, and unparalleled sense of humor.

I owe a great deal of gratitude to my good friend, William Farrell, without who I would have never had the courage to pursue this degree nor the confidence to complete it.

Finally, I am truly indebted to my supervisor, Professor Clifton Johnston, for his continuous support, guidance and unwavering encouragement.

Chapter 1 - Introduction

1.1 Background & Motivation

An aneurysm occurs when a weakening of the arterial wall causes a localized area of the vessel to become enlarged, resulting in an aneurysmal bulge. Aneurysms are most common in the aorta, however they can be located anywhere throughout the cardiovascular system including peripheral, cerebral and coronary arteries. If left untreated the aneurysm could continue to grow and risks rupturing or dissecting, leading to dangerous internal bleeding. The mortality rate for ruptured abdominal aortic aneurysms is 80%, with only half of those who undergo emergency surgery living past 30 days [1]. Aneurysms can remain asymptomatic up until rupture, prompting the implementation of national screening programs in many countries.

Aneurysms had previously been treated using an open repair surgery, however in the last decade percutaneous implantation of a stent-graft has become the preferred treatment for such conditions, with as many as 70% of abdominal aortic aneurysm being repaired using this method [2]. One of principle advantages of percutaneous stent-graft use versus open surgical repair of aneurysm is the elimination of the morbidity associated with large operative incisions.

Stent-graft treatment of aneurysm disease consists of positioning the prosthetic across the affected length of artery, anchoring the graft in healthy vessel proximal and distal to the aneurysm, and re-establishing a normal luminal diameter to guide the flow of blood across the aneurysmal bulge (Figure 1-1). This new channel through the vessel lumen depressurizes the dilated wall of the native vessel which in turn reduces the risk of rupture.

A catheter carrying the constrained stent is introduced into the femoral artery and fed up to the affected vessel. Once the catheter is correctly positioned across the diseased length of vasculature the stent is deployed either by inflating a balloon within the collapsed stent, or in the self-expanding case, by removing an outer-sheath which had been holding the stent in the collapsed position. By restricting the blood's ability to flow into the aneurysmal sack the enlarged section is encouraged to recoil and eventually heal around the graft.

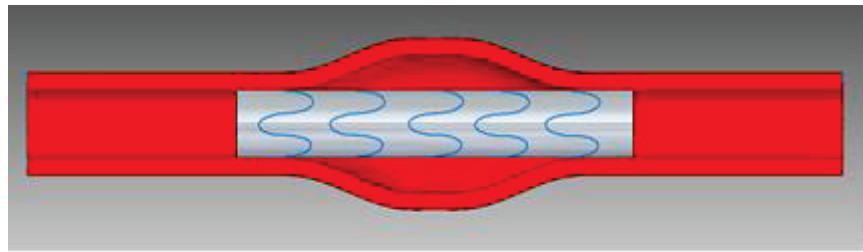


Figure 1-1 – Stent-grafts are used to re-establish a healthy luminal diameter and redirect blood flow across the aneurysmal bulge.

Despite widespread use of stents to treat aneurysms, as well as their convenience of insertion, they remain less effective long-term and lead to a significant increase in secondary interventions as compared to open repair surgery [3], while showing no significant difference in survival after 2 years [4]. This can be attributed to several factors including continued enlargement of the aneurysmal sac, stent migration, dissection, and re-occlusion of the lumen through mechanisms such as intimal hyperplasia and thrombus formation [2].

The primary failure mechanism of a stent-graft is leakage of blood around the stent-graft, a condition known as endoleak. Other complications are associated with local blood flow

disturbances, which have been shown to influence the behavior of the endothelial cells that line the arterial wall. More specifically, shifts in the wall shear stresses from normal biological values, as well as the oscillatory nature of the fluid as it interacts with the vessel wall have been shown to effect the progression of atherosclerosis, the proliferation of intimal hyperplasia and the formation of thrombi [5]. These fluid dynamic considerations directly affect the long-term patency of stent-grafts and have therefore prompted investigation into how the presence of the graft alters the local hemodynamic environment.

1.2 Objectives

Building on past research conducted at the University of Calgary, this project seeks to quantify the changes in flow patterns caused by stent placement and identify which parameters of a stent's design affect fluid disturbances downstream of the graft [6]. Three specific experiments were undertaken, responding to the main research objective:

- 1) Determination of the fluid dynamic effect of individual stent components by measuring changes to velocity profiles, shear stresses and turbulence intensity with a single stent wire followed by 2 and 3 stent wires and a full jacketed stent in an acrylic tube.
- 2) Determination of the effect of oversizing the stent by repeating tests with a 20% and 40% oversized stent as compared to the surrounding vessel, in an acrylic and compliant tube.
- 3) Determination of the effect of the compliance difference between the stent and the native vessel by conducting experiments on a single stent size while varying the compliance of the surrounding silicone vessel.

1.3 Summary

Chapter 2 begins with an overview of past and current stent designs, their uses, failures and the association between those failures and the hemodynamics inside the affected artery. In particular, section 2.5 details past efforts to visualize and quantify such flow patterns, mostly through use of in vitro models imaged using similar methods, however relevant numerical and animal models are also included.

Chapter 3 goes into great detail on the methodology used in this study, especially the specifics of the Particle Image Velocimetry (PIV) set-up and the equations and approaches used parsing data and calculating parameters.

Chapter 4 presents results of the study, broken into 4 sections which correspond to the thesis goals. Section 4.2 demonstrates the capabilities and limitations of the system by performing PIV tests with well understood flow profiles and with no stent present. Section 4.3 continues with the results of studies of the stent wires and full stents in an acrylic tube, under physiological conditions. Section 4.4 repeats this test in an elastic mock artery having a compliance comparable to a healthy adult femoral artery. Section 4.5 compares data taken in tubes of varying compliances using full stents.

Chapter 5 summarizes the findings with a discussion on the implications of these results, particularly the impact of each stent component, oversizing and compliance mismatch. This is followed by a consideration on the limitations of this study. Chapter 5 concludes the thesis with a summary of the findings and directions for future studies seeking to advance the research goals defined in this work.

Chapter 2 – Background & Literature Review: Stent Performance and Limitations

2.1 Introduction

As of a 2007 report, the U.S. Food and Drug Administration had approved 21 balloon-expandable and 28 self-expanding stent designs, with more authorized each year. Some estimates put the number of designs currently on the market or under consideration at over 100, with the balloon-expandable market alone totaling \$4 Billion a year [7, 8]. However, their proclivity to disrupt the normal flow of blood as it passes through the prosthetic remains a concern due to its ability to trigger harmful biological responses [1]. Although the causal relationship between hemodynamic parameters and the proliferation of disease is well established [9, 10], the characterization and quantification of these blood flow disturbances remains an active area of research. This chapter begins with an overview of stent types and characteristics in Section 2.2, as well as how they fail. Section 2.3 details the physiological environment present in an artery and how the altered hemodynamic parameters affect stent efficacy. Section 2.4 examines the significance of a compliance difference between the stented region and native vessel and its role in altering the local fluid dynamics. Section 2.5 describes past investigations and established methods of characterizing flow patterns through stents. Lastly, Section 2.6 concludes the chapter with a summary.

2.2 Overview of Stent Structure and Design

There are an ever-increasing number of stents on the market with designs tailored to specific applications and patient parameters, as well as variability across brands. Although they are usually categorized by their intended location within the human body, such as vascular/non-vascular or coronary/peripheral, it is more useful in the current discussion

to refer to them in terms of their expansion method due to its relevance in material and geometry selection. Self-expanding stents are manufactured in the open configuration, compressed down using an outer sheath and introduced into the vessel percutaneously to the desired location. Once positioned, the sheath can be removed and the stent will expand to its predetermined diameter to fit snugly in the vessel. Such stent designs rely on the elastic properties of the material (typically Nitinol or stainless steel, which have low elastic modulus and a high yield stress) to ensure the device will establish the predetermined diameter once deployed [8]. Conversely, balloon-expandable stents are manufactured in the closed position and are secured over a deflated balloon-catheter. Similar to the self-expanding stents, these are introduced into the arterial system and fed up to the affected region. Once in place the balloon is inflated, expanding the stent and implanting it securely in the vessel, after which the balloon is deflated and removed. Such stents rely on the plastic-deformation of the material to appropriately design the structure and require a material with low yield stress and high elastic modulus.

The geometry and pattern of the stent struts have important implications on their flexibility, expansibility and fluid dynamic ramifications. A trade-off exists in regards to struts between the flexibility of the stent and its radial strength. Additionally, the thickness of stent-struts has been shown to be an important parameter affecting the healing of the arterial wall. A comprehensive review of these considerations is out of the scope of the current work, however Stoeckel, Bonsignore and Duda [8] go into great detail classifying the breadth of strut designs available.

Another important distinction is the difference between stents used in stenotic or aneurysmal vessels (with the latter often referred to as a stent-graft or endograft) and the

considerations that accompany these two applications. In the case of the stenotic vessel, the stent is used to open up a collapsed or otherwise constricted passageway (due to a build-up of atherosclerotic plaque). These stents are often made of a wire mesh. Endografts, contrarily, are used to reline healthy vessels across an area of increased diameter and therefore are generally covered in an impermeable fabric sheath (usually polyester or Polytetrafluoroethylene). These are commonly used to treat aneurysms, particularly in the aorta, iliac and femoral arteries. For the purpose of this study, we will mainly focus the discussion on self-expanding endografts used in the treatment of aneurysms, however, in some cases it may be worthwhile to consider additional stent designs and studies thereof.

The specific characteristics of an endograft varies greatly, with 5 different brands of self-expanding abdominal aortic aneurysm (AAA) stent-grafts approved for use [11]. Most are comprised of a series of stent wires in sequence, sutured to the fabric sheath. Stent-grafts can be straight tubes of uniform cross-section or can be tapered, depending on the location and geometry of the vessel being treated. Endografts can also bifurcate into two smaller diameter stent-grafts, as are commonly used when treating AAAs which require the grafts to extend into the iliac arteries. These types of grafts are often modular to allow more variability in sizing and geometry, depending on the specific anatomy of the patient. For the present study, a Cook Zenith Z-Wire stent-graft was studied which is comprised of three identical stainless steel stent wires sutured to a constant diameter woven polyester sheath (Figure 2-1)

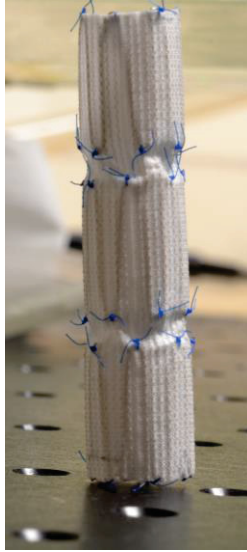


Figure 2-1 - 12mm Cook Zenith Gianturco Stent-Graft.

The main anchoring mechanism at the distal and proximal ends remains the force the stent wires apply on the vessel wall, yet some endografts make use of hooks and barbs to securely fasten the stent in place. Their use remains contentious, however, as they often fully penetrate the arterial wall, possibly causing leaking or rupture. Additionally, these fasteners may also damage the endothelial lining, potentially accelerating intimal hyperplasia [1]. In an effort to secure the graft in place the diameter selected is typically 10-30% oversized as compared to the native vessel. In clinical applications, oversizing is defined as the ratio of the stent's nominal diameter compared to the vessel's outer diameter (OD), however for this study it is defined using the inner diameter (ID), as detailed in Section 3.4. Though such proximal oversizing has been shown to decrease the instances of endoleaks, it has also been associated with other secondary issues such as wall degeneration or dilation [12]. The role of oversizing on stent efficacy remains unclear with conflicting reports in literature, however studies have shown the degree of oversizing can have an important impact on the shear stresses and other fluid dynamic parameters that are known to contribute to in-stent restenosis [10]. The lack of knowledge in this area

leaves clinicians with simplified rules of thumb for selection of appropriate stents for each patient case.

The primary complication arising after graft placement is leakage occurring in or around the treated area, allowing blood to circulate through the aneurysmal sack [1]. A quarter of endografts will experience leaking, with self-expanding stents showing a higher tendency than their balloon-inflated counterparts [13]. Endoleaks are categorized into four types, which are characterized by where and how the leak is occurring.

Type I endoleaks arise due to improper sealing at either end of the graft. These can in part be attributed to anchor sites regularly being compromised, diseased, or too short, thereby leading to poor fixation. This inadequate adhesion coupled with hemodynamic drag can also lead to stent migration, which has been observed in all current graft designs with an overall migration rate of $\sim 2\%$ after one year [1]. The flow of blood into the aneurysmal sac encourages continued enlargement of the vessel, with 21.1% of endoleak cases causing sac expansion [14]. Other types of endoleaks can be due to retrograde flow through branch vessels, mechanical failure of the graft, improper sealing where two graft components meet and porosity of graft material.

2.3 Hemodynamics and Stent Patency

2.3.1 Introduction

Fluid dynamics play an important role in the behavior of arterial tissue, particularly once that tissue has become damaged. To understand how changes to the hemodynamic environment impact vessel health and the long-term healing in areas of stent implantation, it is essential to first understand the complex feed-back system which exists at the fluid-

tissue interface. Section 2.3 begins by explaining the physiological environment within the artery (Section 2.3.2) and subsequently details responses that are triggered once the fluid dynamic parameters have been altered, particularly the WSS (Section 2.3.3 and 2.3.4).

2.3.2 Physiological Environment

Blood is a complex and dynamic fluid which is comprised of both liquid and solid particles, with red blood cells accounting for approximately 40% of its volume [15]. Its viscosity is typically cited between 3.5-4.00 cP, however this is largely dependent on the hematocrit concentration. The shear-thinning nature of blood further complicates assigning a fixed value to blood viscosity, while the pulsatile nature of blood flow additionally encumbers its characterization, with zero and reverse flow present in some arterial segments.

The arterial wall is comprised of three layers; the tunica intima, media and adventitia. The tunica adventitia is the outermost layer of the arterial wall and is comprised mainly of collagen. It provides stability to the vessel, while anchoring it to adjacent organs and structures. The tunica media, or the middle layer of the blood vessel, is comprised primarily of smooth muscle cells (SMC) and elastin. It forms the bulk of the artery's mass and plays the most significant role in determining the artery's mechanical properties. The ratio and arrangement of collagen, elastin, and SMC dictate the elasticity of the vessel, as collagen has a much higher elastic modulus than elastin. Their combined role in the arterial structure causes the compliance to be dependent on the vessel's expansion- as the pressure in the artery increases the compliance of the vessel decreases. This is due to the fact that in the initial phase of stretching the more distensible elastin dictates the mechanical properties, however once a certain diameter is reached the collagen fibers

become fully extended and begin to engage, becoming the dominant component and causing a drop in compliance.

The innermost layer of an artery, a single layer of endothelial cells, is in direct contact with the mechanical forces caused by pulsatile blood flow, particularly the frictional forces which act parallel to the flow known as the wall shear stress (WSS) (Figure 2-2). This monolayer is highly sensitive to changes in these forces and will react to alterations in an attempt to reestablish the native hemodynamic environment and maintain homeostasis. This is done through several mechanisms such as modulating the secretion of vasoconstricting or vasodilating agents, mediating inflammatory responses, aiding or abating the proliferation of SMC, and facilitating the release of procoagulant or anti-coagulant molecules [16].

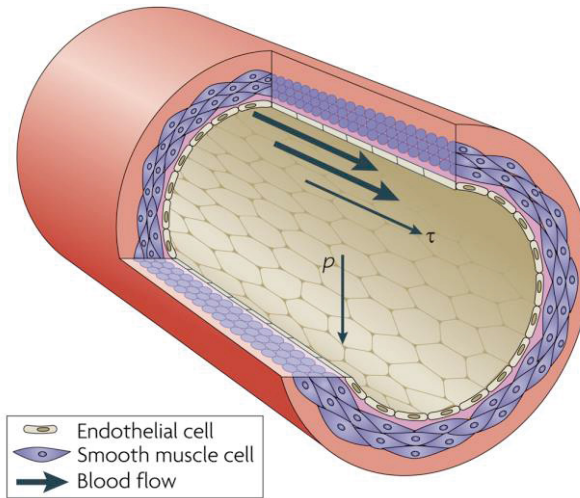


Figure 2-2 - A segment of an artery showing the endothelial monolayer and the forces that act on it, namely the WSS (τ) and the radial pressure (p) [17].

The endothelial cells can also alter the permeability at the lumen-wall interface to selectively allow the transfer of macromolecules between the passing blood and the tunica intima. This characteristic is of particular importance as fluid properties of the passing

blood have been shown to alter the morphology of endothelial cells, reshaping the interface and altering the macro-molecular permeability. Several studies, such as one by Chien [9] have shown that cells exposed to flow with a clear direction remodel and reorient to align themselves with the flow (Figure 2-3), while reversing and oscillating flows add to the deterioration of endothelial performance.

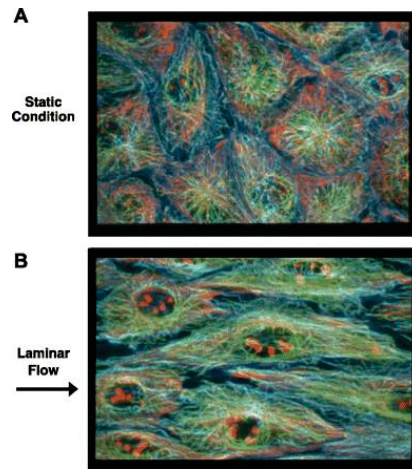


Figure 2-3 - Effect of fluid flow on morphology and alignment of endothelial cells [9].

Secondary complications, particularly stent occlusion, have been shown to have a strong association with the dysfunction of endothelial cells lining the vessel walls. Disease proliferation and damage during stent placement play a role in the malfunctioning of these cells, however strong evidence exists suggesting the hemodynamic environment they are exposed to is a crucial stimulus affecting endothelial behavior [16]. This link between the fluid-structure interactions at the vessel wall and the long-term patency of the stent make investigation of the fluid disturbances caused by stent placement essential to the improvement of endograft treatments.

Vessels treated with both bare stents and stent-grafts risk occluding, causing ischemia downstream of the affected site. Mechanisms attributed to stenosis include calcifications,

the development of atherosclerotic plaques, thrombus formation and intimal hyperplasia, with the latter representing the leading contributing factor to in-stent restenosis [18]. Although some of these mechanisms may be more pronounced in a particular case they work collectively to re-occlude the vessel, creating a complex and interdependent problem. Several of these adverse reactions can occur immediately following stent deployment due to vessel injury sustained during implantation, however most commonly they develop in the weeks and months following the procedure. Figure 2-4 illustrates the relative timeline over which these reactions occur, with each of these occlusion mechanisms considered in detail in the sections that follow.

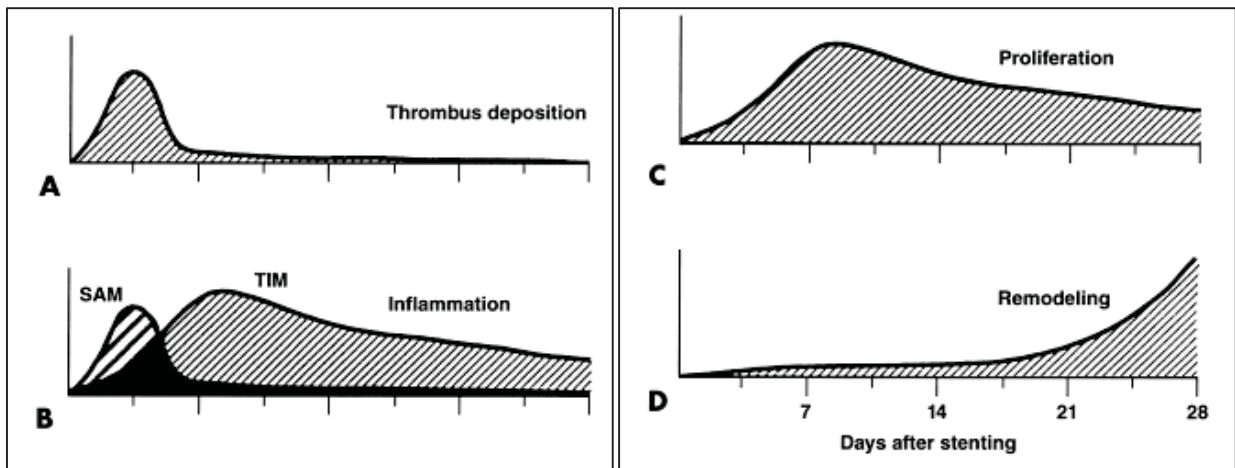


Figure 2-4 - Illustration taken from Edelman & Rogers [19] showing the phases of vascular repair which are the crucial mechanisms associated with a narrowing luminal diameter in the weeks after stenting. SAM and TIM refer to surface-adherent monocytes and tissue-infiltrating monocytes, respectively.

2.3.3 Vascular Remodeling and Intimal Hyperplasia

Vascular remodeling is an adaptive process in which the geometry, structure and tone of a vessel will change in response to an altered hemodynamic environment. These changes

are permanent structural transformations of the arterial wall and not simply a prolonged vasodilation or constriction of the smooth muscle [20].

Intimal hyperplasia, a mechanism of the vascular remodeling process, is the thickening of the tunica intima as a response to trauma sustained at the arterial wall. Consequently, the vessel wall will thicken, decreasing luminal diameter and obstructing blood flow. Although injury to the vessel during stent placement is an important factor in prompting vascular remodeling, it is a process regulated by the endothelium and is therefore sensitive to WSS alterations. It will also affect local vessel compliance and extensibility, causing further fluid disturbances [21]. Intimal thickening is characterized by the proliferation of smooth muscle cells through the media and into the tunica intima. This proliferation often occurs between and over struts and with time completely isolates the stent from passing blood flow.

A decrease in local WSS has been shown to correspond to a decrease in luminal diameter, while increasing WSS increases luminal diameter [22]. This mechanism serves the crucial role of maintaining a consistent baseline flow rate when other changes occur within the circulatory system. Many studies have assessed this relationship between hemodynamic alterations and vascular remodeling. One such study by Langille & O'Donnell of the carotid artery in rabbits found that a 70% reduction rate of blood flow, which is directly proportional to the WSS, resulted in a 21% reduction in luminal diameter after 2 weeks [20]. Di Stefano et al. found that doubling the flow rate in the carotid artery of rabbits caused a 15% increase in the luminal diameter after 12 weeks as compared to a control group. Shear stresses observed in the experimental group did not differ from the control group despite vascular remodeling, suggesting that given a healthy artery this is an

effective mechanism for maintaining constant shear within the vessel [23]. In humans this mechanism attempts to maintain a mean shear stress within the 15-20 dynes/cm² range [16].

2.3.4 Atherosclerotic Plaques & Thrombus Formation

Atherosclerosis is characterized by plaque deposits in the vessel wall, which are typically composed of lipids and white blood cells. Although this is usually thought of as a buildup within the luminal surface, atherosclerotic lesions are actually an accumulation between the tunica intima and media. Once a lesion is formed it can develop into a stenosis or can weaken the arterial wall, causing an aneurysm. These plaques can remain stable, or can continue to grow, partially occluding the lumen and disrupting blood flow. If left untreated a vulnerable plaque may rupture, releasing thrombogenic materials into the blood stream and possibly causing a complete blockage downstream. Although the causes of atherosclerosis are multifactorial and not yet fully understood, lesions are known to develop in specific areas of the vasculature, particularly around bifurcation and curvatures, suggesting that the local fluid dynamics play an important role in their development [24].

Atherosclerotic lesions have been shown to develop in regions of low and oscillating shear stresses [16], with a WSS below 5 dynes/cm² promoting atherogenesis [25]. These areas have increased residence times at the fluid-vessel interface, causing an increase in the uptake of particles through the endothelial layer, particularly lipoproteins. Furthermore, as endothelial cells are known to change their morphology and orientation in response to alterations in the WSS, areas of disturbed or abnormal flow alter the absorbency at the wall and further promote the progression of atherosclerosis [24].

Despite areas of high WSS being atheroprotective, high WSS can destabilize existing plaques, provoking rupture. A plaque rupture sends procoagulant materials into the blood stream triggering thrombosis (blood clots). Thrombus may remain attached to the vessel wall, partially or fully occluding the stent or can travel downstream tissue or organ ischemia.

In addition to plaque rupture, thrombi can form through several other mechanisms, with uncharacteristic shear stresses (both high and low) shown to encourage coagulation. When tissue is damaged, the primary response is for platelets circulating through the bloodstream to attach to the affected region and then subsequent platelets will aggregate at the active site. Although this is beneficial for limiting blood loss after trauma, in regions of atypical flow patterns, such as in the vicinity of a stent, this mechanism may be triggered unnecessarily. Abnormally high shear stresses have been shown to damage platelets, provoking their activation and the release of procoagulant microparticles, which work together to prompt and further encourage platelet accumulation [26, 27].

The role WSS plays in the appearance and progression of atherosclerosis and clotting remains a complex problem, with both an increase and decrease in its magnitude producing potentially catastrophic consequences.

2.4 Compliance Mismatch

Arterial compliance is a measure of the vessel's elasticity and describes its ability to distend with increasing internal pressure. The presence of stent struts will cause local perturbances in the velocity patterns of the vessel, however disturbances can also be

attributed to a compliance difference between the native vessel and the stented portion of vasculature due in part to the increased impedance as the fluid passes through the stent. In addition to disturbing the hemodynamic environment, this compliance mismatch can promote stent migration and endoleaks due to device separation. It has also been shown to have important implications on circumferential stresses experienced by the vessel.

It is well established that this compliance mismatch plays an important role in the development of intimal hyperplasia and other occlusive diseases in end-to-end and side-to-end anastomoses, both with synthetic and harvested grafts [28, 29]. Despite being a widely accepted phenomenon in vascular grafting, compliance mismatch is seldom explored in relation to stenting, though the mechanism by which the compliance discontinuity affects vascular grafting, through damage to the endothelial cells, is analogous in stent-grafts. Of the studies conducted on stent-grafts, compliance mismatch has been shown to cause changes in hemodynamic parameters, altering the pressure and velocity gradients [30, 31, 32].

An analytical model by Alderson & Zamir evaluated the hemodynamic effect of stent stiffness, length and position within the vessel [30]. It was concluded that the stiffer stent within a more compliant vessel increased the pressure proximally, while lowering the pressure distal to the stent. This pressure differential is positive in the direction of the flow, aiding fluid through the stented portion of the vessel. This effect is more pronounced with increasing length of the stent.

A computational fluid dynamic (CFD) analysis by Selvarasu et. al examined the fluid-structure interactions of a compliance mismatch in a simulated coronary artery with pulsatile flow. Changes to the WSS and oscillatory shear index (OSI) were found to be as high as 9% and 15% respectively, given a ten-fold increase in compliance in the stented regions [32]. However, this study neglected the stent's physical presence in the artery and the narrowing of the lumen, focusing entirely on the vessel stiffness discontinuity.

A study by Surovtsova et al. considered the fluid dynamic and solid mechanic implications of a compliance mismatch using an analytical approach and concluded that the abrupt change reduces the peak value of WSS. Tortoriello et al. [33] studied the implications of a compliance mismatch using numerical methods and found that the discontinuity produces more intense negative WSS within the stent with quickly changing WSS at the ends. Additionally, these effects are amplified when accompanied by a slight decrease in luminal diameter.

Berry et al. [31] developed a compliance matching stent (CMS) and characterized its properties using a numerical finite element modelling (FEM) simulation as well as an in vivo swine model. By comparing this novel design to a standard Palmaz stent, it was concluded that the CMS produced less solid mechanical stresses in the native artery as well as limited hemodynamic disturbances. Histology from the swine model revealed limited thrombus and inflammatory cell accumulation, implying that smoothing the transition from artery to stent could yield better long term patient outcomes.

2.5 Stent Induced Blood Flow Disturbances

Given the strong association between blood flow patterns and the progression of harmful responses within the vessel, the effect of graft placement on local fluid dynamics has become an expansive area of research. However, efforts made to visualize flow patterns as they pass in and around the stents have largely been limited to numerical simulations (which have several limitations when attempting to replicate *in vivo* flow) or simplified experimental investigations [7]. Most notably, existing work often neglects the effects of the moving walls and very few studies take into account the non-Newtonian nature of blood flow, a characteristic that has been shown to have an important impact on results. Gijssen et al. [34] used FEM simulations coupled with a Laser Doppler Anemometry (LDA) study to investigate the influence of non-Newtonian considerations in the carotid bifurcation. They observed prominent differences between the Newtonian and non-Newtonian models, and noted the importance of including the shear thinning behavior when studying hemodynamics. Similarly, Walker, Johnston and Rival [6] found that neglecting non-Newtonian characteristics underestimated WSS, while increasing spatial coverage of flow reversal.

Even scarcer are experimental flow studies including a covered stent-graft, with the majority of studies being limited to bare-metal or drug-eluting stents. Furthermore, studies of the flow in the large arteries, such as the iliac and femoral remain limited, with the much smaller coronary arteries being the focus of the majority of research of this type.

An early study by Natarajan et al. [35] used PIV coupled with numerical simulations to investigate flow disturbances downstream of simulated stent. The flow was treated as

Newtonian and water was used as the working fluid. The walls were modeled as rigid and the stent was idealized using two polished acrylic rings in sequence implanted inside the test section. A decrease in WSS was noted at the wall, while an increase was observed at the peak of the simulated stent's protrusions. Recirculation zones in the valley between the simulated stent struts were observed with corresponding flow separation and re-attachment, inciting low shear stresses.

Similarly, Peacock et al. [36] used an in vitro pulse duplication system and a model of the aortic root and left anterior descending/left circumflex coronary artery to confirm flow disturbances induced by slotted (Johnson & Johnson) and spiral (Cook) stents. The experiments were repeated in both a rigid and a flexible test section. Flow instabilities were detected 1 cm downstream under mild exercise conditions, with no fluid dynamic changes detectable at 5 cm downstream. The spiral stents (which have a larger diameter) were shown to create more disturbances and agitate the flow at lower Reynold's numbers. Surprisingly, no differences were noted between the flexible and rigid test sections. Additionally, WSS was observed to increase upon introduction of the stents.

Greil et al., undertook similar investigations using a Laser Doppler Anemometry (LDA) system and a silicon mold of the carotid bifurcation at a Reynolds number of 250 [37]. Stents (Wall-stents by Boston Scientific) were placed in four configurations within the internal carotid artery, in both correct positions and in positions simulating stent displacement. The velocity changes of each were measured, in addition to a non-stented baseline case. Stent placement was not found to have a significant effect on flow in the internal carotid artery, but flow was considerably disturbed in the external carotid artery.

They concluded that the stents location and size must be carefully selected to reduce blood flow disturbances.

A 2010 study by Chankro et al. [38] used PIV to study the changing WSS in 3 mm diameter (0.4 mm wall thickness) compliant Sylgard[®] 184 vessel implanted with a 6.67% oversized Abbott XIENCE stent. These stents are coronary, drug-eluting, unsheathed stents with a significant structural difference from the Gianturco stents under consideration in this study, however the method of study is almost identical. The stent configurations were a non-stented flow, baseline case, over-expanded, two overlapping stents and increasing stent length. The flow was a Newtonian mixture of glycerol and water (40%-60%). Overall a decrease in WSS was noted after stent-implantation, however minimal variation was observed between various cases. Pertinently, the change in length did not have an appreciable effect on the parameters. Although an overall drop in OSI was observed, the authors note that no clear correlation exists between OSI and WSS. A 2009 study by the same authors, using the same test set up, compared the effects of four brands of DES [XIENCE V[®] (Abbott Vascular), TAXUS Liberté[®] (Boston Scientific), Endeavor[®] (Medtronic), and Cypher[®] (J&J Cordis)] and found that the differences in design played a substantial role in the local hemodynamic disturbances, although all were found to cause a decreases in WSS within and downstream of the stent.

A similar DPIV study by Yazdani et al. [39] investigated the effects of compliance mismatch on flow parameters using a 12 mm Sylgard[®] vessel implanted with a rigid cylindrical insert (simulating the extreme zero compliance case) and a 13mm Cordis SMART Stent. The authors concluded that the compliance difference had an impact on

flow induced disturbances and vortical structures, with the lower compliance implant causing higher residence times and larger ring-vortices.

Experiments conducted by Walker, Johnston & Rival [6] provide the starting point for this work. In a 2012 study, a similar test set-up and experimental parameters were used to quantify flow passing through the same model Gianturco Zenith stent. However, previous work considered only a single stent wire removed from the polyester cover implanted in a rigid acrylic tube. Additionally, the 6.35 mm wide test section and corresponding stent wire were significantly smaller than the 10 mm diameter test section being assessed in the current work. As such, the pulse profile differed substantially to reflect profiles common in larger arteries, including a period of flow reversal not included in past work. The authors observed a drop in velocities close to the wall, with an associated increase in core flow. Additionally, a decrease in WSS was noted upon introduction of the stent wire.

Morris, Stefanov and McGloughin [40] conducted a study using the same model Zenith stent-graft implanted in a rigid acrylonitrile butadiene styrene (ABS) mock-artery of the aorto-iliac bifurcation, coupled with a corresponding CFD model. They found that implantation resulted in a 54% decrease in compliance and 21% increase in the pulse wave velocity.

LaDisa et al. constructed a three-dimensional CFD model of a canine coronary artery after introduction of a slotted tube stent and was used to evaluate the stents ability to alter the WSS proximal, distal and within the stent [41]. It was concluded that stent introduction lowered WSS, while increasing spatial coverage of low WSS at the stent

outlet. At the outlet the WSS dropped by 51% at peak flow under normal conditions and 77% at peak systole for an elevated blood flow case.

A 2005 LDA study by Greil et al., characterized the flow at the exit of a MembraX (Abbott Vascular) stent, which is a nitinol stent with a semi-permeable membrane, as well as a nitinol SelfX (Abbott Vascular) stent and a stainless steel WallStent (Boston Scientific) [42]. The test artery was a silicone mold of the carotid bifurcation, with the stent deployed within the internal carotid artery. No changes were found at the inflow of the stents. The bare stents showed disturbances at the outflow, however the flow recovered within four millimeters of the stent exit (1.33 radii). The covered stent caused a large increase in the velocities at the central slipstreams and disturbances continued much farther from the stent exit, with a maximum intensity occurring at 10 mm from the stent exit (3.33 radii).

2.6 Conclusion

The association between stent-graft failures and hemodynamic disturbances has been well documented in literature, although the exact mechanisms through which this occurs remains a complex and active area of research. Alterations of the WSS and OSI are known to incite harmful changes in the biochemical environment, while further changing the morphology and response of endothelial cells which regulate molecules traversing the arterial wall. This has prompted numerous studies which quantify and qualify exactly how various stent designs, parameters and implantation techniques modify local and regional fluid dynamics. However, modeling these complex physiological environments, both through numerical and experimental methods, remains a challenging undertaking that requires simplifications to be made. This thesis seeks to advance previous work by

incorporating several intricacies which have previously been neglected, most notably the elastic properties of the vessel wall, the addition of subsequent stent wires, and the inclusion of the polyester cover which is a vital part of the Gianturco Stent.

Chapter 3 – Methodology: PIV Experimental Set-up and Image Acquisition

3.1 Introduction

This chapter describes all materials and methods used in the construction of the test section, the collection of PIV images and all data processing. Section 3.2 details the components of the flow loop and PIV system and the overall system integration and structure. Section 3.3 explains the preparation and characterization of the non-Newtonian blood analog. Section 3.4 outlines the method established to construct mock arteries over a range of elasticities and the technique developed for determining their elasticities. Section 3.5 demonstrates how images were processed and vector fields extracted using PIVLab. Lastly, Section 3.6 lists equations and models for calculating subsequent parameters from the velocity profile.

3.2 Experimental Set-up Overview

A closed flow loop was designed and constructed for visualization and measurement of flow through a 10 mm inner diameter tube, representing a simplified geometry of the femoral artery (Figure 3.1) [43]. A common non-Newtonian blood analog, representative of physiological hemodynamic parameters, was circulated through the test section. The mixture was driven through a custom pump with a 1 Hz pulsatile flow profile typical of the human femoral artery [44] .

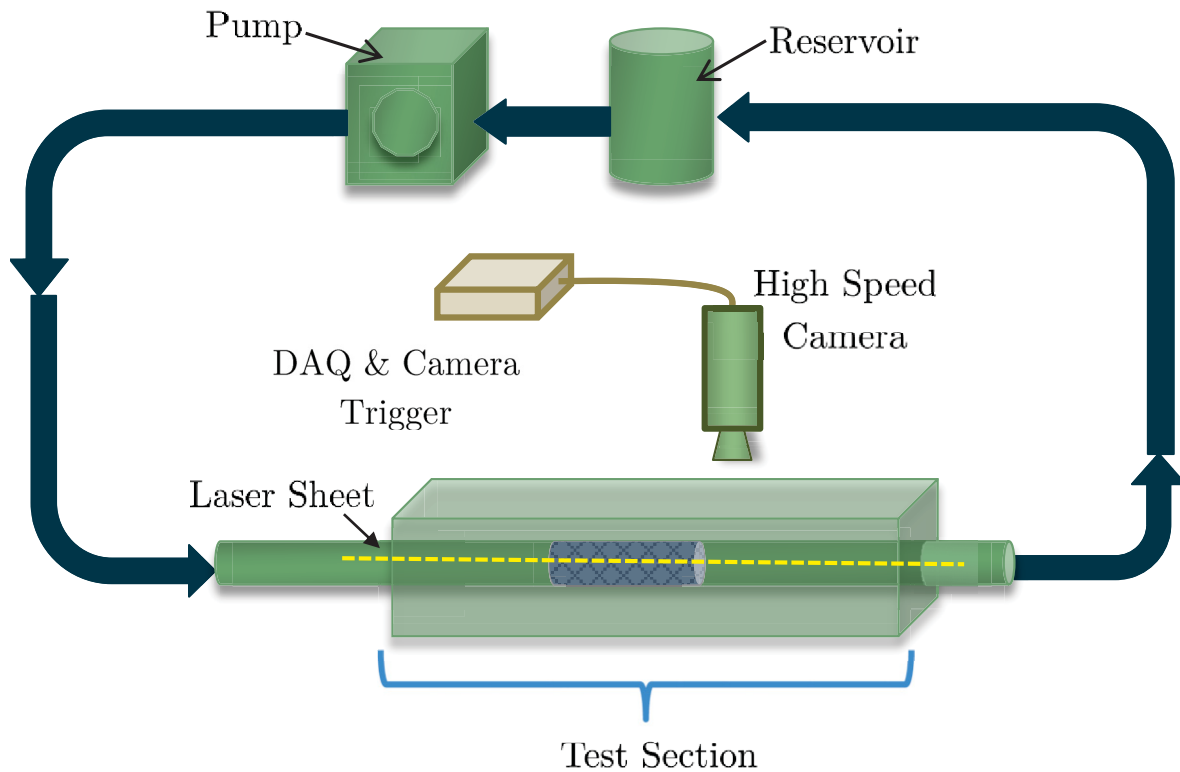


Figure 3-1 - Schematic representation of experimental flow loop simulating arterial blood flow and PIV image acquisition system.

Using Particle Image Velocimetry (PIV), cross-sectional velocity downstream of a Gianturco Zenith stent-graft (Cook Medical, Inc., Bloomington, IN, USA) was quantified. The test section was embedded in an acrylic flow chamber, which was filled with 100% glycerol to correct for the refraction index differences and allow the laser sheet to reach the test area unaffected. The chamber was then fixed to a 2-axis translational stage with a micrometer drive (Thorlabs, Newton, NJ, USA).

The fluid was seeded using 10 μm silver coated hollow glass spheres (Potter Industries Inc., Carlstadt, NJ, USA), which were illuminated using a 1 mm thick laser sheet. The laser sheet was created using an N-Series DPSS laser system (Dragon Lasers,

ChangChung, Jilin, China), and passed through a 50 mm Focal Length (FL) PCX lens, followed by a -12.5 mm FL cylindrical lens (Edmund Optics, Barrington, NJ, USA), spaced 50 mm apart. The laser sheet was positioned at the center axis of the tube, orthogonal to the camera (Figure 3-2).

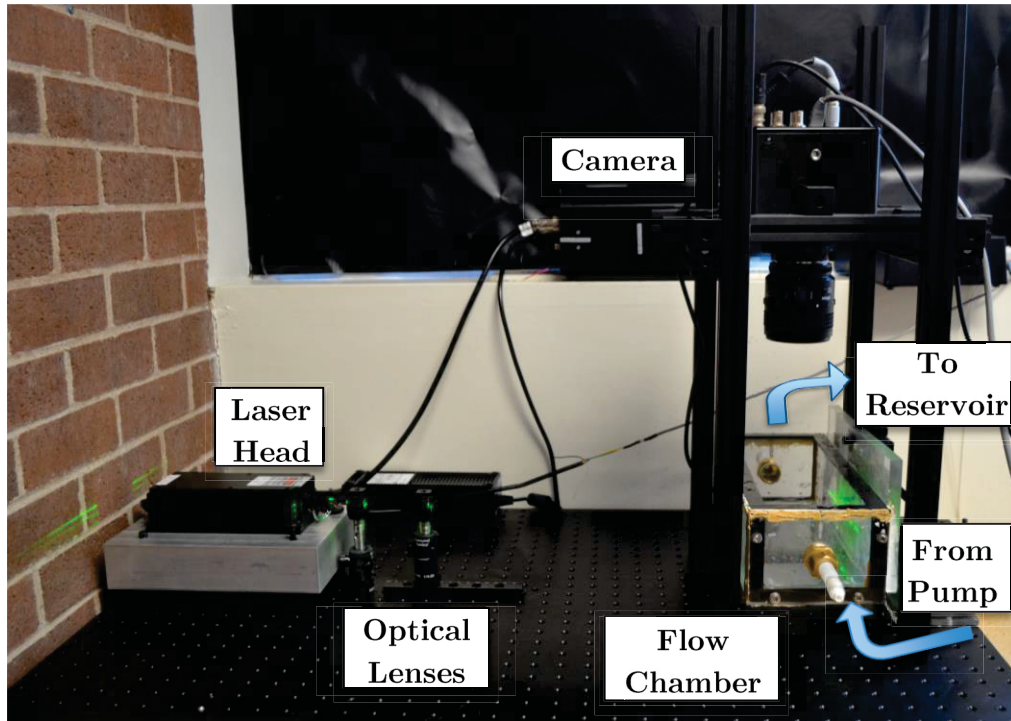


Figure 3-2 – View of experimental PIV set-up constructed for image acquisition of flow through test chamber. Arrows indicate direction of flow.

Image frames were collected using a Photron mini UX100 at 4000 fps with 20 evenly spaced image pairs collected per pulse, over 10 pulses. A Nikkor AF 60 mm Micro lens was used (Nikon, Chiyoda, Tokyo, Japan) with a focal length of 2.8D. Image acquisition was synchronized and triggered to coincide with the start of the pulse using an NI DAQ and custom LabVIEW 2013 routine (National Instruments, Austin, Texas, USA).

Images were first collected for a baseline flow with no stent in the test section, followed by one stent wire, two wires, three wires, and a full jacketed 12 mm stent. A line was drawn across the stent cover to ensure they were oriented consistently (orthogonal to the camera) for each set-up and that the stent wires did not rotate upon placement. Bare wires were removed from the covering of a 12 mm stent, deployed in the test section and aligned as they would be in a full stent (**Figure 3-3**).



Figure 3-3 – Three 12 mm stent wires removed from their polyester cover and deployed inside a 10 mm inner diameter compliant mock artery.

3.3 Blood Analog Fluid and Flow Properties

A common non-Newtonian blood analog representative of physiological hemodynamic parameters was used, comprised of a mixture of glycerol (40%), xanthan gum (0.04%) and water [45]. The fluid's viscosity was confirmed using a pipe flow set-up over a range of steady flow rates. The fluid was circulated through a 6' long, 8.7313 mm ID length of brass tubing using a WT3000-1JB Micro Gear Pump (Longer Pump, Hebei, China). Two pressure transducers mounted 122 cm (~280r) apart recorded the change in pressure across this length. The fluid travelled through a 16.64 cm long section prior to the first pressure

sensor to ensure the flow was fully developed. The entrance length required was calculated for the maximum flow rate under consideration using equation (3.1):

$$L_e = 0.06 * D * Re \quad (3.1)$$

where D is the tube diameter and Re is the Reynolds number. Due to the fluid being non-Newtonian, the velocity profile is not perfectly parabolic and the viscosity can therefore not be calculated using the Poiseuille equation directly. To account for elevated shear strain rates near the wall induced by non-Newtonian properties, the Weissenberg-Rabinowitsch correction (3.2) was used:

$$\gamma_c = \frac{4Q}{\pi R^3} \left[\frac{1}{4} \left(3 + \frac{d \ln \gamma_a}{d \ln \tau} \right) \right] \quad (3.2)$$

where γ_c is the corrected shear strain rate, Q is the flow rate, R is the tube radius, γ_a is the apparent shear strain rate and τ is the shear stress at the wall. Using this corrected shear rate the viscosity was found using equation (3.3):

$$\mu_c = \frac{\tau}{\gamma_c} \quad (3.3)$$

The viscosity was calculated over a series of flow rates ranging from 257.1 ml/min ($Re = 104$) to 2571 ml/min ($Re = 1041$), which corresponded to shear rates of 80.8 s^{-1} and 808 s^{-1} respectively. The blood analog was confirmed to be a shear thinning fluid with a dynamic viscosity at infinite shear, $\mu_\infty = 6.07 \text{ cP}$ (Figure 3-4), which corresponded to previous characterizations of the fluid [45, 6]. Although the viscosity at infinite shear is slightly high in relation to physiological conditions, this mixture ensured adequate index matching and non-Newtonian behavior.

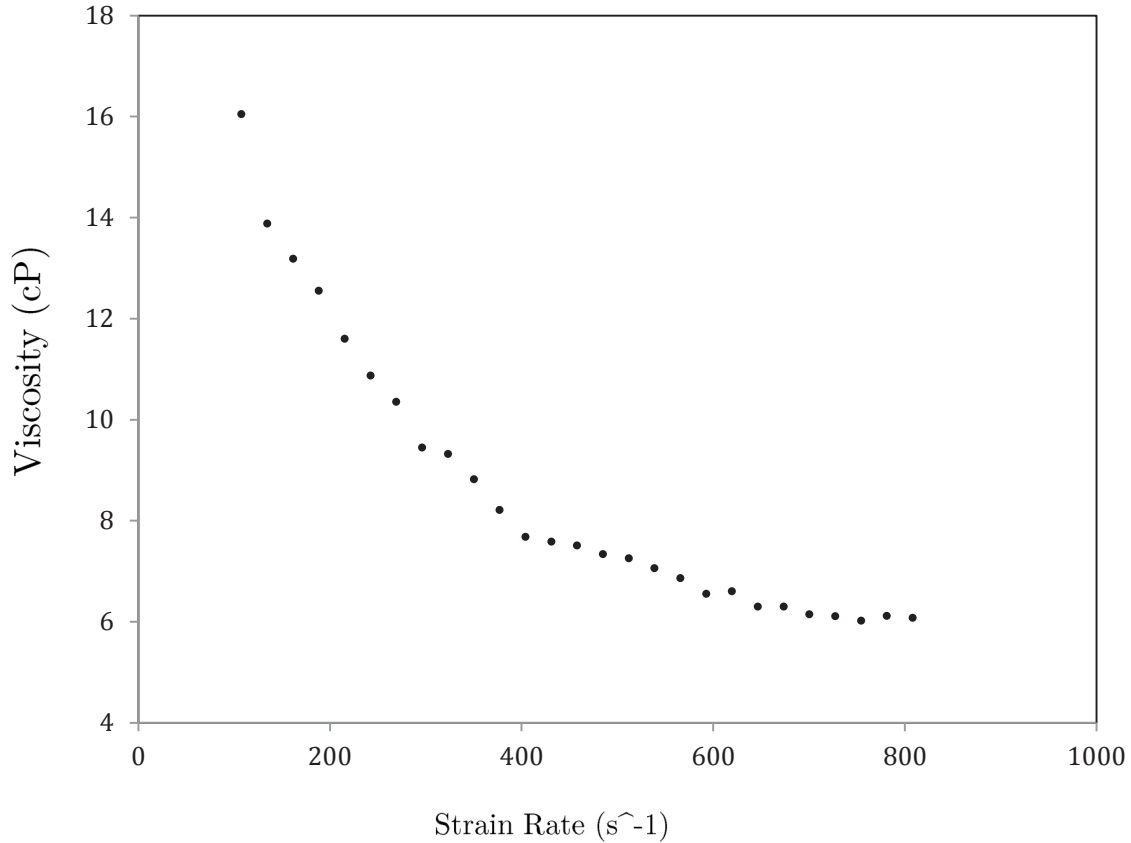


Figure 3-4 – Viscosity calculations across a range of strain rates for the Glycerol-Water-Xanthan mixture measured using a pressure drop pipe set-up.

The pulse shape (Figure 3.5) was adapted from Ku [46] and the mean velocity at peak flow was chosen as 47 cm/sec, the mean peak forward velocity in the femoral artery reported by Fronek et al. [47]. This corresponds to a Reynolds number at peak flow of 1033.5, which is within the physiologically observed range [48]. The Womersley number was calculated to be 4.7, which is comparable to in vivo values in this artery [48, 49]. The pressure at the tube entrance was recorded using a Honeywell 40PC sensor and was found to be 82 mmHg at peak pulse, which is slightly low for in vivo matching.

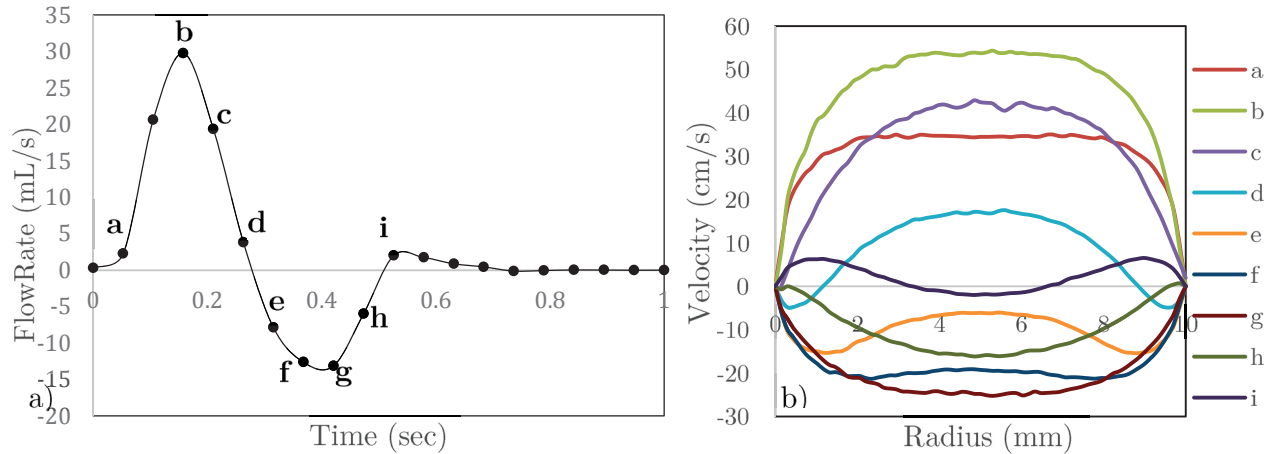


Figure 3-5 – a) Typical 1 Hz flow profile in the femoral artery adapted from Ku [46]; b) Velocity profiles across pulse cycle recorded by PIV measured at $x/R=0.5$ from stent exit.

The custom pump was tuned to produce this profile and measurements recorded from the pump’s encoder were compared to ensure its consistency. Comparing two runs with changing parameters downstream, the average percent difference at peak pulse introduced by piston movement as recorded by the encoder was 5.27%. Once the required profile was attained the pump’s setting were not altered for any test. All pump settings and parameters used can be found in Appendix B.

3.4 Mock Arteries

As the stent under consideration was a 12 mm Gianturco stent and given that stents are typically oversized by 10-30 %, a 10 mm ID was chosen to represent an artery. Although in clinical practice the oversizing is defined using the OD, we define it using the 10 mm ID as the thickness of the mock arteries was selected to modulate the compliance and ensure the artery could be affixed securely to the test section. As such the value of the OD is meaningless in this context and it is the ID that will have important fluid dynamic implications. This should not have any impact on results as the change in thickness as the vessel expands will be negligible compared to the diameter of the vessel.

All tests were first run using an extruded acrylic tube with an internal diameter of 10 mm and an external diameter of 13 mm. Mock arteries were then custom manufactured to test stents in an elastic tube with compliances comparable to human arterial tissue.

A custom three-part mold was manufactured to cast tubes with a 10 mm ID and ½” OD (Figure 3-6). The mold is comprised of two inch thick steel bars, which serve as the top and bottom of the mold, with ¼” deep 14” long trough with a semi-circular cross-section milled into each. At either end of both troughs are rectangular recesses where the mandrel sits. As the mandrel is in contact with the inner surface of the tube, the critical region for this research, a precision ground stainless steel rod was used. Alignment pins were added on either side of the mold.

Sylgard® Elastomer 184 (Dow Corning, Midland, MI, USA) is a common material used to approximate human tissue, particularly in arterial models due to its material properties being comparable to physiological values. Additionally, this silicone product is optically transparent, which will allow the flow inside to be viewed and imaged directly. Furthermore, the refractive index ($n = 1.4118$) is very close to that of the surrounding glycerin ($n = 1.4115$), meaning the laser sheet can reach the fluid unaltered. Tubes of different compliances were created by varying the base to curing agent ratio. The components were measured by weight using a one milligram precision scale and mixed thoroughly.

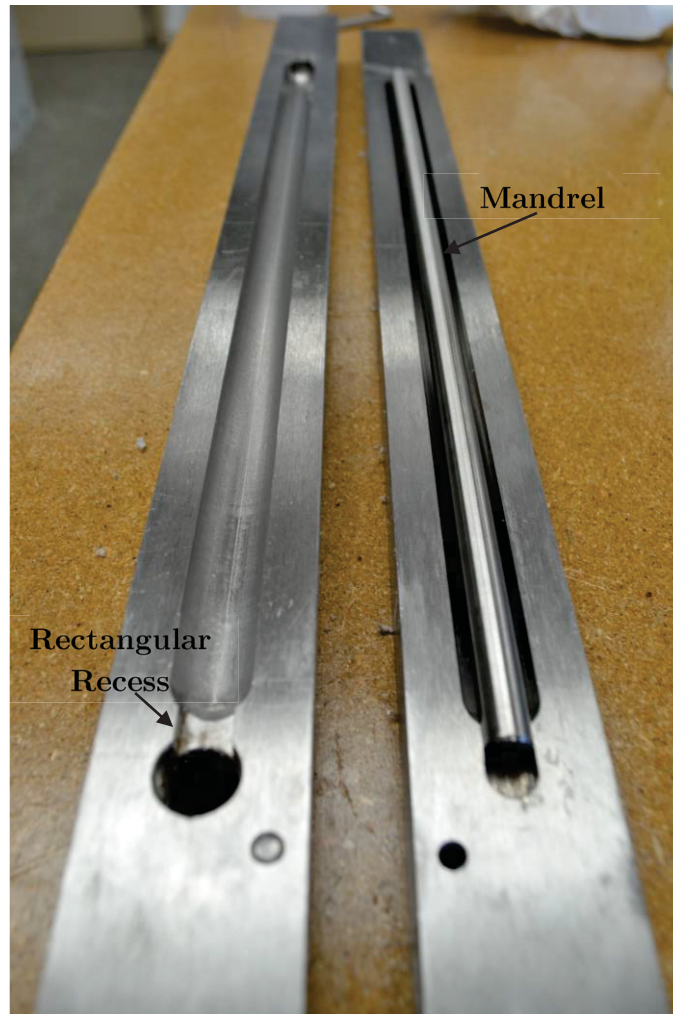


Figure 3-6 – Three part machined steel molds used to manufacture silicone mock arteries.

The Sylgard[®] mixture was then degassed in a vacuum chamber at 30 mmHg for 30 minutes to remove any air bubbles introduced during the mixing procedure. The mixture was visually inspected to ensure all the air was removed and additional degassing time was added if necessary. The silicone was then poured into the assembled mold and the set-up inclined at a 45° to allow any trapped air to escape. The mold was then placed in a precision oven at 100°C for two hours. Once cured, syringes were used to inject acetone between the luminal rod and the Sylgard[®] tube and the tube was carefully slid from the mandrel.

The Sylgard tubes were guided over brass rods and affixed using heat-shrink sleeves, Teflon tape and zipties to ensure there was no leaking at the connection. The brass rods were threaded to easily connect inside the acrylic box (**Figure 3-7**). The box was filled with glycerol, completely immersing the tube and rendering it effectively imperceptible to the laser sheet.



Figure 3-7 - Sylgard vessel affixed in acrylic test section

The compliance of each Sylgard[®] tubes was tested and compared with physiological values. Compliance describes the vessel's ability to distend with increasing internal pressure and is defined as:

$$C = \frac{(\Delta V)/V_0}{\Delta P} \quad (3.5)$$

where ΔV is the change in volume, V_0 is the original volume, and ΔP is the change in pressure. This method of characterizing a vessel's elastic properties is a simplified model

as there is a non-linear relationship between the volume and pressure that is dependent on the composition of the particular vessel wall and its geometry. Additionally, arterial tissue is an anisotropic material that is affected by chemical and biological responses. As such there are range of compliances that exist for any given artery and is further contingent on age and sex. Clinically, compliance is often reported as the percentage change in diameter for a given change in pressure, with units of $\% \text{ mm Hg}^{-1} \times 10^{-2}$. Tai et al. [50] used an ultrasound wall tracking system, while simultaneously recording brachial pressure to measure the femoro-popliteal compliance in subjects with and without peripheral vascular disease. The mean compliance of the common femoral was found to be $6.2 \% \text{ mm Hg}^{-1} \times 10^{-2}$ and $14.1 \% \text{ mm Hg}^{-1} \times 10^{-2}$ in the diseased group and healthy age-matched control group respectively.

All compliance measurements were taken with the Sylgard[®] tubes mounted in the acrylic box and surrounded by glycerol exactly as they would be during PIV testing. The tube was then attached to a three-way Luer-Lock valve. One end of the valve was attached to a Honeywell 40PC pressure sensor (Morristown, NJ, USA), while the other was attached to a 0.1 ml increment syringe. The tube and syringe were filled with seeded glycerol and an initial pressure measurement was recorded. Glycerol was then injected into the tube in one-milliliter increments by the depressing the syringe, while simultaneously recording pressure change for each incremental volume increase. The PIV set-up was modified to record a single image for each change in pressure, which was then used to determine the change in diameter. Measurements were taken along a four-inch length of tube to determine if edge effects resulting from the tube being fastened at each end impacted the results. No difference in diameter was visible between the center of the tube and either end. As such all diameters used for compliance measurements were taken at the center of

the tube. The diametrical compliance was calculated and compared to clinically observed values using the equation:

$$C (\% \text{ mm Hg}^{-1} \times 10^{-2}) = \frac{\Delta D / D_0 \times 10^4}{\Delta P} \quad (3.6)$$

where ΔD is the change in diameter midway across the tubes length and D_0 is the diameter of the unpressurized tube. Six catalyst ratios were measured, which are summarized in Table 3.1 along with their measured compliances. Of the six tubes tested, three were selected for use in PIV measurements. The 10:0.5 yielded a close compliance to that measured by Tai et al. in the healthy control group and was therefore selected as the baseline compliance for all tests. An elevated compliance of $12.92 \% \text{ mm Hg}^{-1} \times 10^{-2}$ and a lower compliance of $6.2 \% \text{ mm Hg}^{-1} \times 10^{-2}$ were selected for comparison as they fell within the clinically observed range. The three compliances will be referred to as C_{High} , C_{Base} , and C_{Low} .

Table 3-1 - Measured compliance of mock arteries of varying base to curing agent ratios

Base : Curing Agent Ratio	Compliance ($\% \text{ mm Hg}^{-1} \times 10^{-2}$)
10 : 0.200	154.77
10 : 0.340	28.81
10 : 0.420	12.92
10 : 0.500	7.77
10 : 0.600	6.20

3.5 Image Acquisition and Processing

The PIV images were processed using PIVLab [51], using a multi-pass cross-correlation algorithm with a 50% window overlap and final interrogation window size of 32 x 32 pixels. The field of view allowed for measurements up to 3R from the stent exit, yielding a pixel density of 2×10^{-5} m/px. A region of interest (ROI) was selected using the PIVLab GUI at the inner walls of each tube, an example of which is shown in Figure 3-8(a). Instantaneous velocity vector fields (Figure 3-8b) were averaged for each time point to obtain 20 vector maps across the pulse for each stent arrangement.

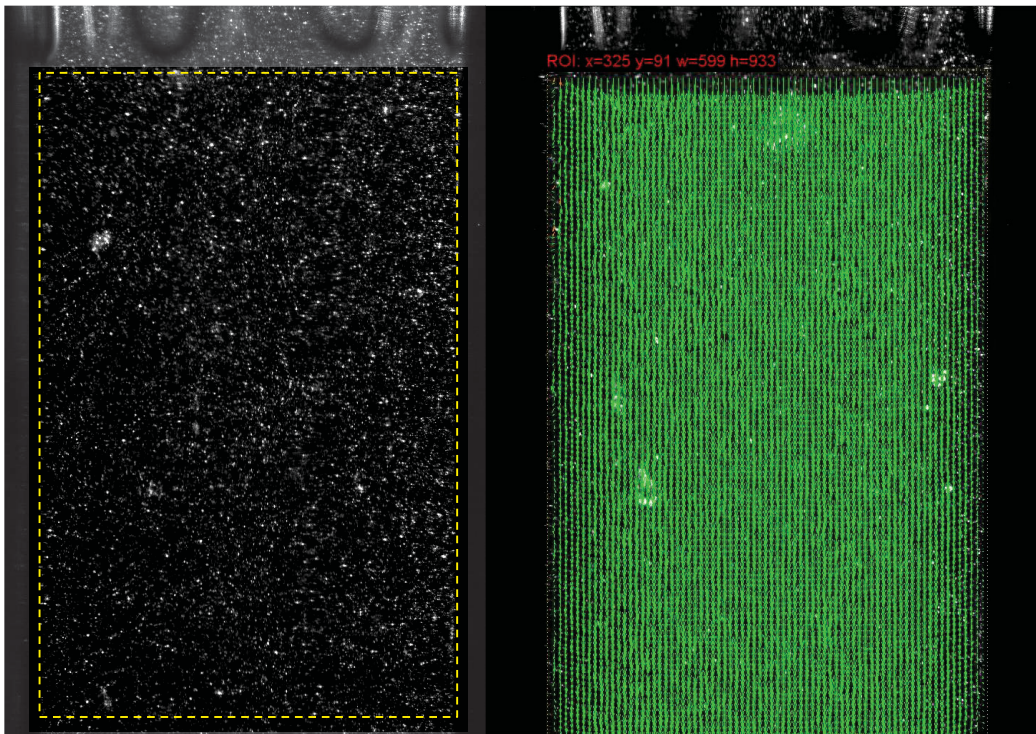


Figure 3-8 – a) PIV image acquired using Photron Mini UX100 of a Sylgard[®] tube at the exit of a single stent wire. Yellow dashed lines indicated the selected ROI; b) Vector field output for a single frame sequence.

In the case of the compliant arteries, a tapering effect was observed after implantation of the graft, which complicated selection of the ROI (Figure 3-9). To account for this, the

ROI was selected at peak flow (the largest expansion of the radial diameter) and unnecessary vector rows were deleted manually after vector field processing. The expansion of the vessel was found to be consistent across pulses, making the removal of vector rows reliable. Table 3-2 summarizes the inner diameter of the tube after stent implantation immediately downstream of the graft, in an unpressurized tube.

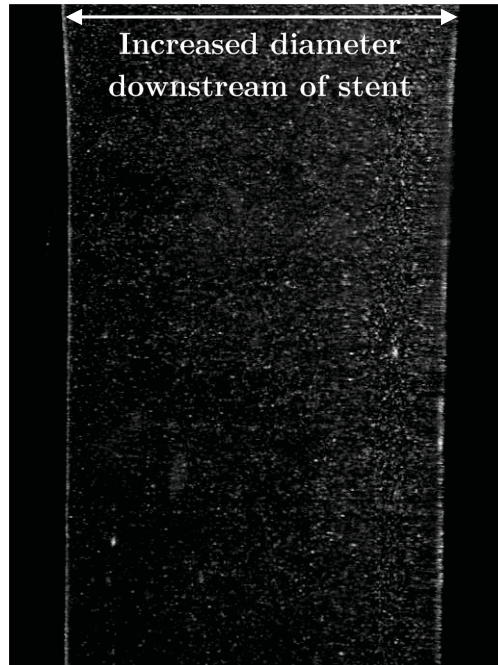


Figure 3-9 - PIV image of a 12 mm stent implanted within a silicone mock artery at resting flow, illustrating the expansion in luminal diameter and tapering downstream of the stent.

Table 3-2 Inner diameter at stent exit after implantation of a 12 mm and 14 mm stent-graft for 3 compliances of elastic arteries at zero flow.

	Compliance % $\text{mm Hg}^{-1} \times 10^{-2}$	12 mm Stent	14 mm Stent
C_{Low}	6.2	10.3352 mm	10.4493 mm
C_{Base}	7.77	10.5451 mm	10.6653 mm
C_{High}	12.92	11.0484 mm	11.1569 mm

3.6 Data Processing

Once vector fields were extracted using PIV lab and averaged for each time point, all parameters were calculated and displayed using custom MATLAB 2013 (MathWorks, Natick, MA, USA) routines, the codes for which can be found in Appendix A. The WSS for a Newtonian fluid is defined as the product of the viscosity (μ) and the local shear strain rate (γ):

$$\tau = \mu * \gamma \quad (3.7)$$

However, non-Newtonian fluids have shear rate dependent viscosity, meaning this equation cannot be used directly to find the WSS. The Carreau-Yasuda model is therefore used to find the corrected non-Newtonian viscosity:

$$\mu_y = \mu_\infty + (\mu_0 - \mu_\infty) * [1 + (\lambda\gamma)^2]^{\frac{n-1}{2}} \quad (3.8)$$

where μ_0 is the viscosity at zero shear, μ_∞ is the viscosity at infinite shear, γ is the shear strain rate, λ is the relaxation constant, and n is the power index. Values used were adapted from Walker [6]. The shear strain rate was defined as the slope of the velocity gradient and was found by fitting a linear regression to the two vectors radial from the wall to determine the slope of the velocity profile.

The oscillatory shear index (OSI) gives an indication of flow reversal, with an OSI of zero indicating a unidirectional flow. It was calculated using equation (3.9), as proposed by Ku et al. [46].

$$\text{OSI} = 0.5 * \left(1 - \frac{\left|\int_0^T \tau dt\right|}{\int_0^T |\tau| dt}\right) \quad (3.9)$$

where $\left|\int_0^T \tau dt\right|$ is the sum of all the WSS (both positive and negative) and $\int_0^T |\tau| dt$ is the sum of the absolute values of the WSS.

Measures of disturbances considered were the turbulence strength, the turbulence intensity.

The turbulence fluctuation at a point is defined as the difference between its instantaneous velocity, v_i , and the average velocity \bar{v} (equation 3.10).

$$v'_i = v_i - \bar{v} \quad (3.10)$$

The turbulence strength at that point is the standard deviation of these fluctuations, while turbulence intensity is that value divided by the average velocity.

Chapter 4 – Results

4.1 Introduction

PIV results are presented beginning in section 4.2 with the validation of the experimental set-up by quantifying a known flow, as well as comparing data from the PIV and the pump's encoder.

Results are then divided into three sections. Section 4.3 details experiments performed using different stent components in the rigid acrylic tube. This is followed by the same experiments repeated in a compliant silicone mock artery ($C_{Baseline}$) in Section 4.4. Lastly, section 4.5 contains results of experiments conducted over a range of vessel compliances using full stents.

4.2 PIV Validation and Calibration

4.2.1 Steady Flow of Water in Acrylic

Water was circulated through the rigid acrylic test section at 354mL/min (the mean flow rate in the femoral artery [43]) and imaged using the PIV system. The velocity profile observed was compared to analytical values predicted by the Poiseuille equation (equation 4.1) to validate the accuracy of measurements taken with the PIV system. The velocity profile, $v(r)$, of Poiseuillian flow follows the equation:

$$v(r) = 2 * v_{max} \left(1 - \frac{r^2}{R^2}\right) \quad (4.1)$$

where R is the total radius of the tube (5 mm in the current case). The curve showed good agreement with the model, with an average percent error of 1.94% as compared to analytical values (Figure 4-1).

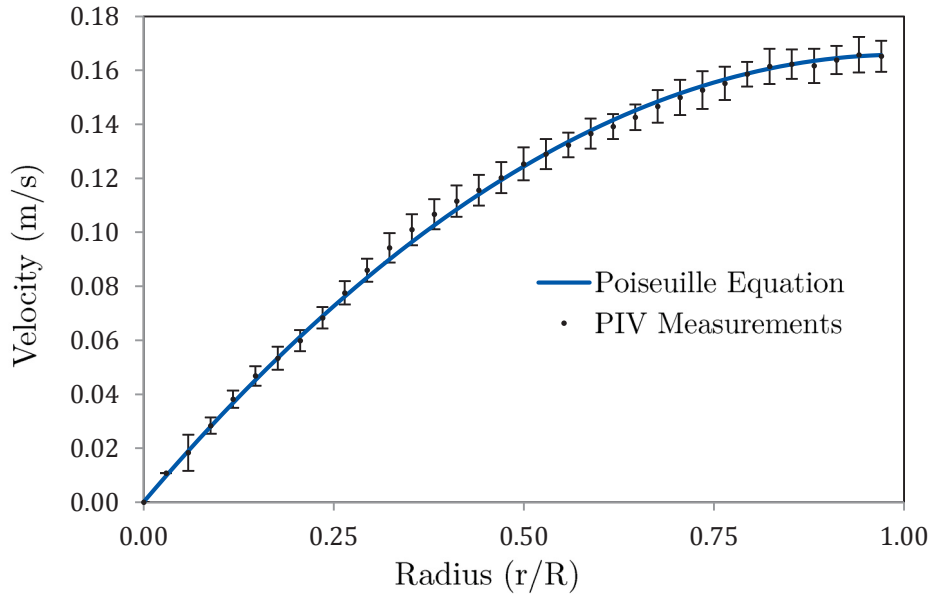


Figure 4-1 - PIV measured velocity profile in non-stented steady flow through a rigid acrylic test section compared to the Poiseuillian flow estimation. Error bars represent standard deviations of velocity measurements.

4.2.2 Steady Flow of Non-Newtonian Analog in Silicone

Steady flow PIV testing was performed over a range of flowrates in the rigid acrylic tube, as well as the baseline compliant Sylgard[®] mock artery ($7.7 \% \text{ mm Hg}^{-1} \times 10^{-2}$). The glycerol-xanthan blood analog was used as the working fluid and the results compared to measurements acquired in the acrylic tube to ensure flow was fully developed upon reaching the test section. Velocity profiles in the Sylgard[®] tube followed a parabolic trajectory comparable to that of the acrylic experiments for all flowrates measured (from 354ml/min to 2400 ml/min). Measurements at the mean flowrate of 354 ml/min are shown in Figure 4-2.

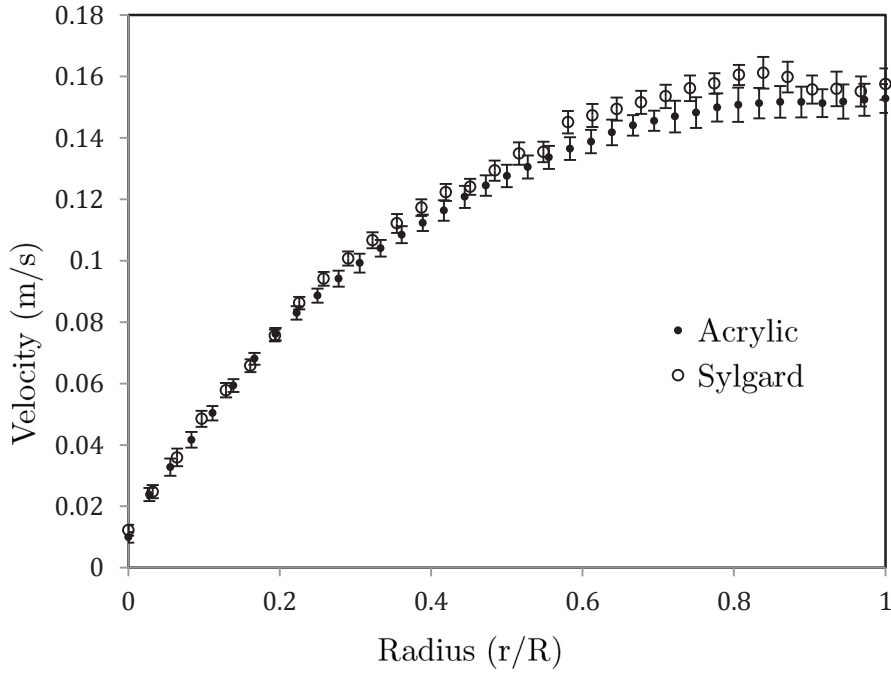


Figure 4-2 - PIV measured velocity profile in non-stented steady flow through a rigid acrylic test section and a compliant mock artery (C_{Base}) at a flow rate of 354 ml/min using a blood analog. Error bars represent standard deviations of velocity measurements.

4.2.3 Non-Newtonian Analog under Pulsatile Flow

The non-Newtonian analog was subsequently exposed to pulsatile flow and the custom pump was tuned to obtain the desired pulse shape and frequency. Once the required profile was attained the pump's setting were not altered for any test. All pump settings and parameters used can be found in Appendix B. Recordings of piston velocity logged by the pump's encoder were multiplied by the pistons' area to obtain the flowrate at the exit of the pump. The flowrates measured using the PIV were compared to values calculated using the encoder's piston (Figure 4-3). The actual flowrate agreed with the encoder data at all points, with the exception of the flow at peaks where the acceleration changed direction, which was consistently higher than that predicted by the encoder. This is to be expected as the fluid will have some momentum at these points, while the piston's

motion is forcibly altered. This effect was consistent and was taken into account while tuning the parameters to ensure the actual flow occurring in the test section matched physiological values.

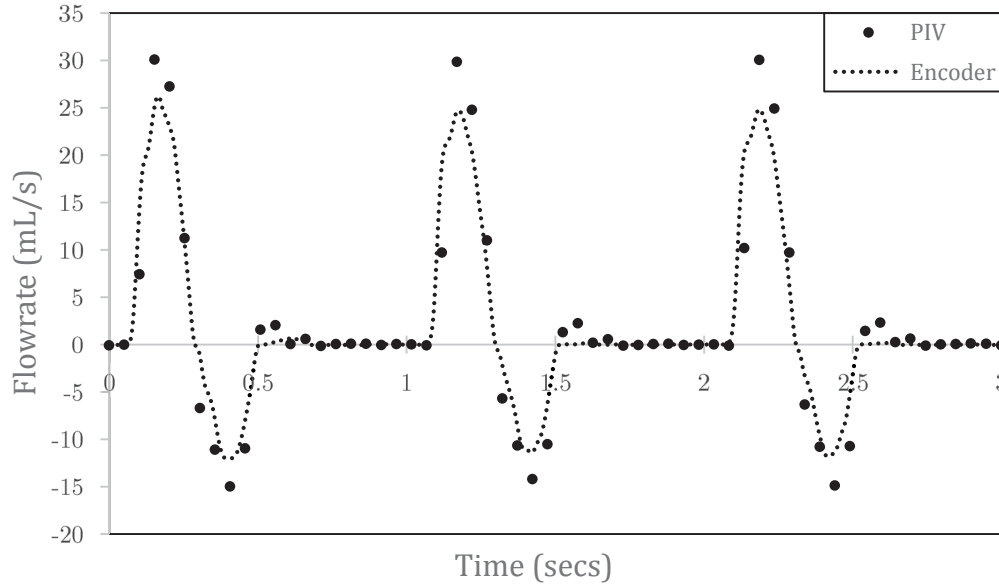


Figure 4-3 - Flowrates calculated based on instantaneous piston velocities compared to those obtained from PIV data

All PIV measurements acquired using the non-Newtonian analog exposed to pulsatile flow were collected over 10 pulse cycles and averaged. Figure 4-4 is the average flow profile of all runs conducted in acrylic (no stent, 1 wire, 2 wires, 3 wires, 12 mm full stent, and 14 mm full stent) and the associated standard deviations. The volumetric flow rate, Q , was found by calculating the volume under the 3-dimensional velocity profile using the double integral in equation 3.4;

$$Q = \int_0^\pi \int_0^{2r} v r \, dr d\theta \quad (4.2)$$

where $v(r)$ is the axial velocity as a function of radius. The shell method was used to calculate this integral from PIV vector fields. The pulse was determined to have the largest deviations at locations in the cycle where the slope was larger and the flow was therefore changing quickly, while the peaks of the pulse had smaller deviations. The largest standard deviation of the custom pump occurred at the sixth time-point and was determined to be 1.8 mL/s.

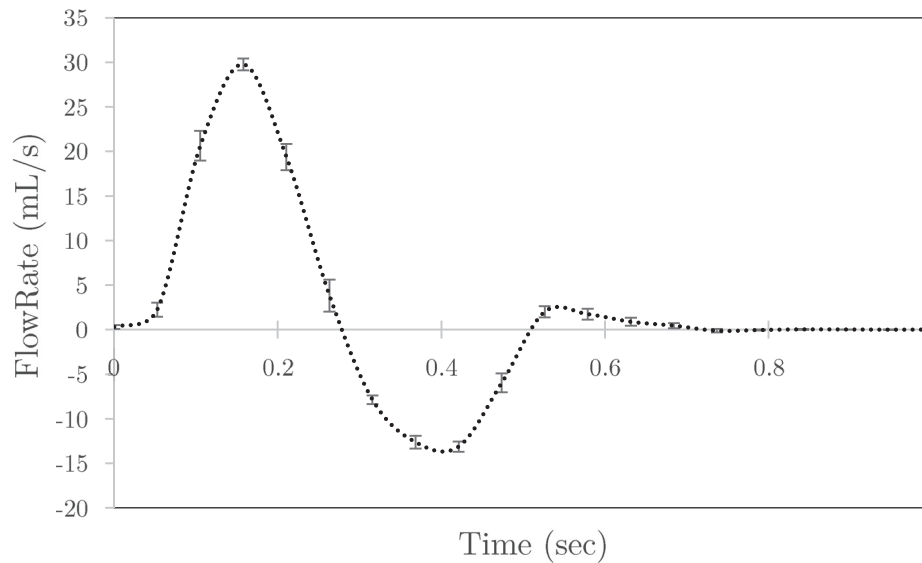


Figure 4-4 – Pulse flow rates averaged over 10 pulses in acrylic tube for all stent configurations. Error bars represent standard deviations of flow measurements in mL/s for the six test configurations.

4.2.4 Pulsatile Flow in Elastic Tubes

The non-Newtonian analog was circulated through three elasticities of compliant Sylgard® vessels with no stent in the test section. The changing diameter of the tube introduced several fluid dynamic complexities, most notably the instantaneous flowrate at the peak pulse now being contingent on the elasticity of the vessel. This is due in part to the capacitive nature of the vessel, where some volume is stored during peak pulse due to the

radial expansion of the test section, decreasing the flowrate at that point in time. This effect was more pronounced in the higher elasticity vessels as it expanded to a larger radius and therefore a larger volume of fluid was being stored for each pulse.

For these cases, the flowrate can no longer accurately be quantified using shell integration due to the emergence of a radial velocity component, however axial flowrates can be found. The volume stored at peak pulse was estimated by measuring the radial expansion in the PIV pictures and simply multiplying the area change by the length of the elastic portion of the flow loop. These measurements, as well as the peak axial velocities for each elasticity are summarized in Table 4-1.

Table 4-1 - Axial flowrates and volume stored at peak pulse for a range of test section elasticities under pulsatile flow conditions using a non-Newtonian blood analog.

	Peak Axial Flowrate (mL/s)	Volume stored at peak pulse (mL)
Acrylic	30	0
C_{Low}	24.4	1.34
C_{Base}	23.3	2.25
C_{High}	19.4	4.6

The radial velocities increase with increasing compliance due to larger increases in diameter. As the radial velocities are very small and do not add to the shear stresses at the wall, all results will be reported using the axial velocities. As each compliance has a different baseline axial flowrate, all velocity measurements have been normalized using the maximum velocity at peak flow in a non-stented vessel for that particular vessel compliance.

Due to the vessel's diameter now varying throughout the pulse cycle, the velocity profiles at baseline conditions (with no stent present) differ from those in the acrylic section (with a constant diameter of 10 mm). At peak pulse the diameter increases and therefore the velocity must decrease correspondingly to maintain continuity with respect to the flowrate.

The diameter at peak pulse for the baseline compliant tube was measured from the PIV image and was found to be 10.516 mm. This corresponds to a theoretical decrease in peak velocity of 10.6%, if radial velocity is neglected. Figure 4-5 shows the measured velocity profiles in the acrylic and Sylgard[®] test sections, where the change in peak velocity is 8.4%, within range of the analytical value one would expect. The small discrepancy in the values is the portion of energy which has now been transferred to the radial velocity.

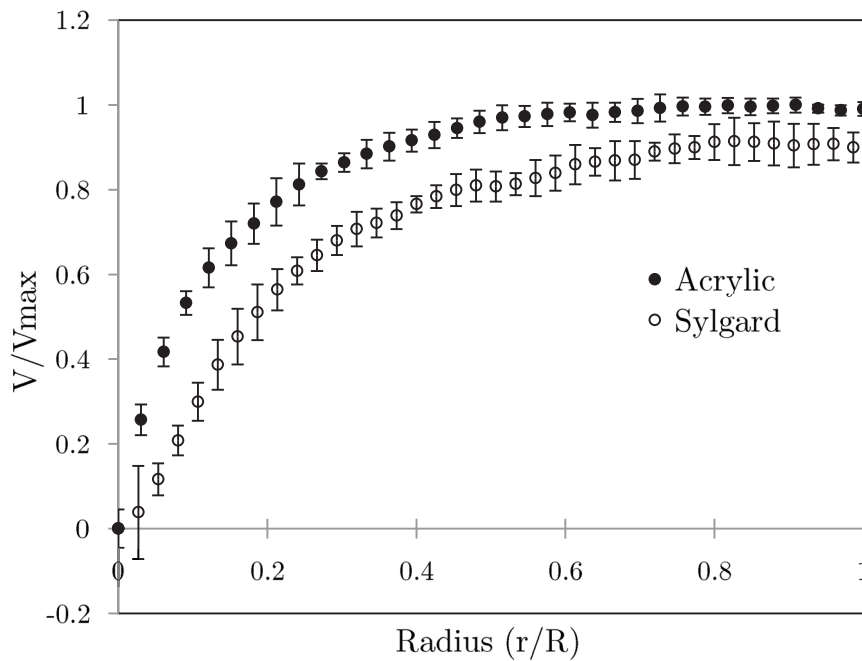


Figure 4-5 – Peak velocity profiles measured in rigid acrylic tube and compliant Sylgard[®] mock artery with no stent. Error bars represent normalized standard deviations. All velocities are normalized using maximum velocity in the acrylic tube.

Interestingly, as the compliance of the non-stented vessels increased, so too did the WSS. Although it is apparent from Figure 4-5 that the strain rate at the wall (which is directly proportional to the WSS) has decreased in the compliant tube, the shear thinning nature of the fluid causes the viscosity to increase drastically at lower shear rates. This non-Newtonian behavior dominates at the wall, causing an overall increase in the local WSS. Table 4-2 summarizes these changing parameters for each vessel, showing the large increase in average WSS in the compliant tubes.

Additionally, the OSI decreases in the more compliant tubes. The flow in the acrylic, non-stented tube is already very oscillatory due to the reverse flow present in the femoral artery (Table 4-2). The decrease in the elastic tubes can be attributed to the fact that at the peak of the pulse the WSS has jumped drastically, causing a more positive WSS over the course of the cycle.

Table 4-2 - Cycle averaged WSS and OSI for three compliant and one rigid tube using a non-Newtonian blood analog under pulsatile flow conditions.

	Oscillatory Shear Index	Cycle Averaged WSS
Acrylic	0.439	0.920
C_{Low}	0.289	6.64
C_{Base}	0.187	9.64
C_{High}	0.214	7.53

4.3 Acrylic Tubes

4.3.1 Individual Stent Wires

The introduction of a single stent wire slightly lowered the velocity at the near wall, while accelerating the flow in the middle of the tube, with centerline velocities at $x/R=0.5$ increasing by 4.65% (Figure 4-6). The largest change, a 5.306 cm/s (20.4%) drop, occurred 0.7332 mm from the wall. The changing parameters near the wall caused a drop in the local shear strain rate at most points in the cycle, prompting a decreasing in WSS (Figure 4-7). The most drastic changes of WSS occurred during acceleration of the flow, with the largest change occurring at 0.45s (with a change of 136%). At peak flow, the WSS decreased by 22.0%. Flow was re-established within one radius from stent exit at peak pulse. The introduction of a second and third wire had no discernable effect on velocity values downstream of the stent (Figure 4-8).

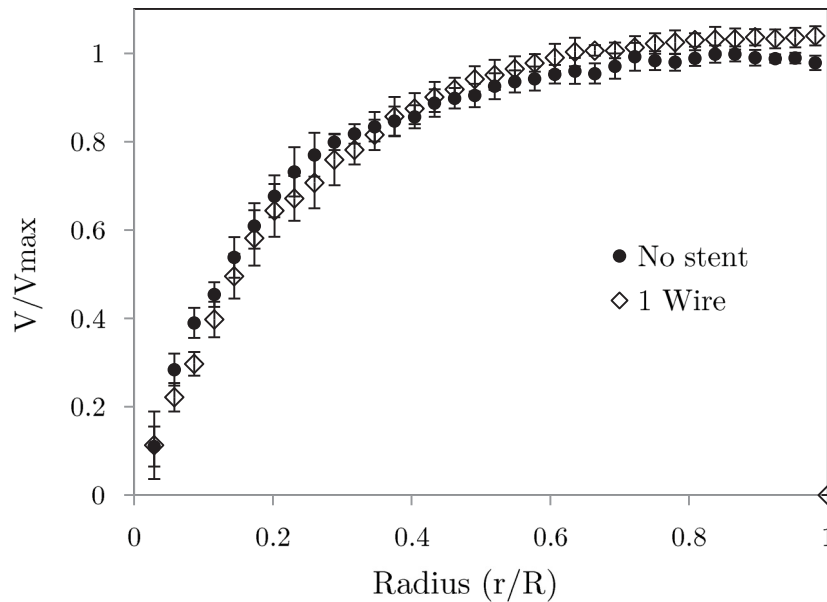


Figure 4-6 –PIV velocity measurements (normalized using the maximum velocity of the no stent case) from near-wall to tube center measured at $x/R = 0.5$ from outlet of a single stent wire compared to non-stented flow in a rigid acrylic tube.

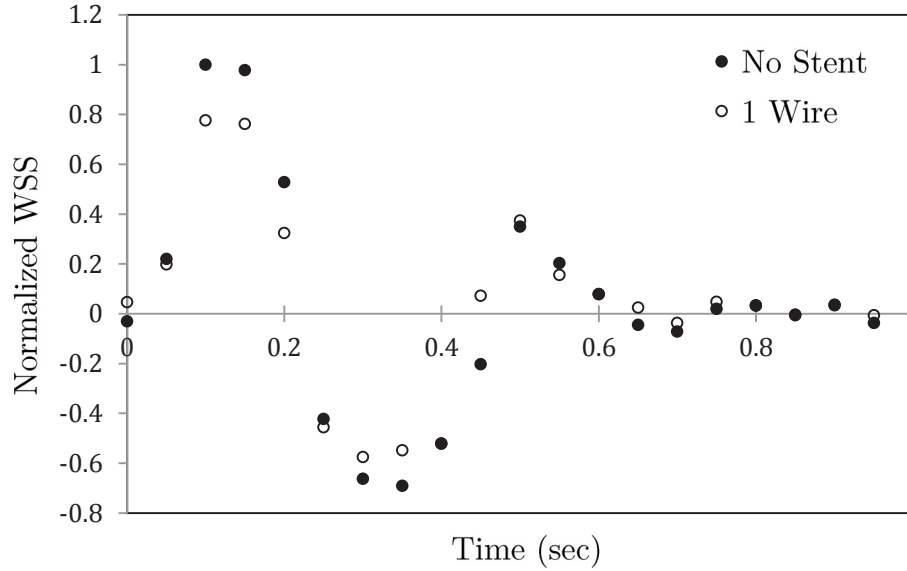


Figure 4-7 - Normalized WSS in single wire stented flow across pulse cycle at $x/R = 0.5$ from stent outlet compared to non-stented flow.

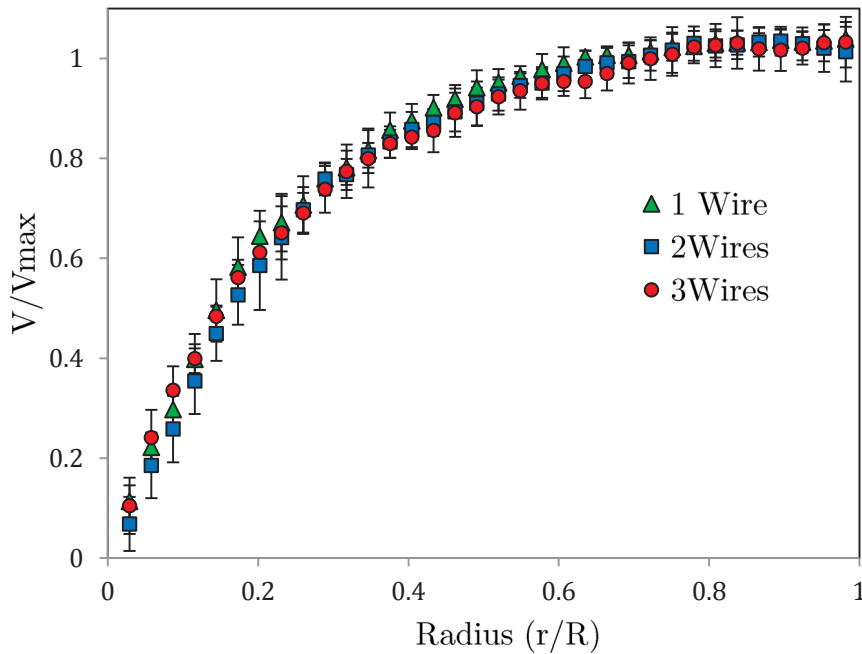


Figure 4-8 - PIV velocity measurements (Normalized using maximum velocity of no stent case) from near-wall to tube center measured at $x/R = 0.5$ from outlet of a three stent wire configurations in a rigid acrylic tube. Error bars represent normalized standard deviations.

4.3.2 Full Stents

Introduction of a full stent (3 wires in a polyester cover) had a substantial effect on flow velocities, particularly at peak pulse. Unlike measurements collected without the cover, the flow observed followed an asymmetric pattern due to variations in the folding and pillowing of the fabric between the stent wires. This asymmetry was more pronounced in the 12 mm stent. This appears to be due to the fact that the 12 mm stent has seven wire peaks, while the 14 mm stent has eight. Although both were installed in the tube such that their wires were symmetric in the plane of the camera, the seven peaks allowed more intra-wire spacing and therefore allowed the fabric sheath and wires to deploy asymmetrically and increase variations in the flow patterns. The eight wire peaks had more coverage at the wall, allowing less variation in fabric folds between the wires with a more even deployment of the peaks and consequently a more uniform flow pattern.

Both stents caused a considerable reduction in velocity close to the wall accompanied by an accelerated core flow (Figure 4-9). At 20% and 40% oversizing (12 mm and 14 mm stents) the centerline velocities at $x/R=0.5$ increased by 65.4% and 86.2%, respectively, as compared to the non-stented condition. At peak pulse, the 12 mm stent caused a velocity reduction from the wall to $r/R = 0.5776$ and $r/R=0.7040$ to the far wall, with flow reversal noted between the wall and $r/R= 0.08664$. A similar pattern was observed with the 14 mm stent, with reduced velocities occurring between the wall and $r/R = 0.4621$ and $r/R= 1.5306$. The largest absolute change for both stents occurred at $r/R=0.2310$ and was a decrease of 35.60 cm/s (85.0%) and 31.72 cm/s (75.8%) for the 12 mm and 14 mm stents, respectively.

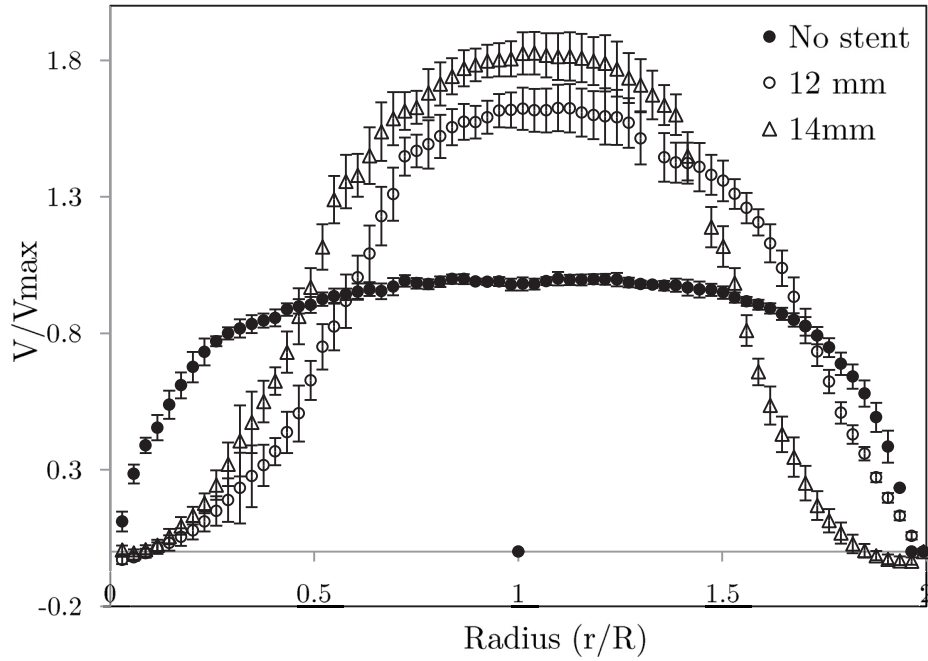


Figure 4-9 - Normalized PIV velocity measurements across entire diameter measured at $x/R = 0.5$ from stent outlet for a 12 mm and 14 mm full stent at peak pulse in a rigid acrylic tube. Error bars represent normalized standard deviations.

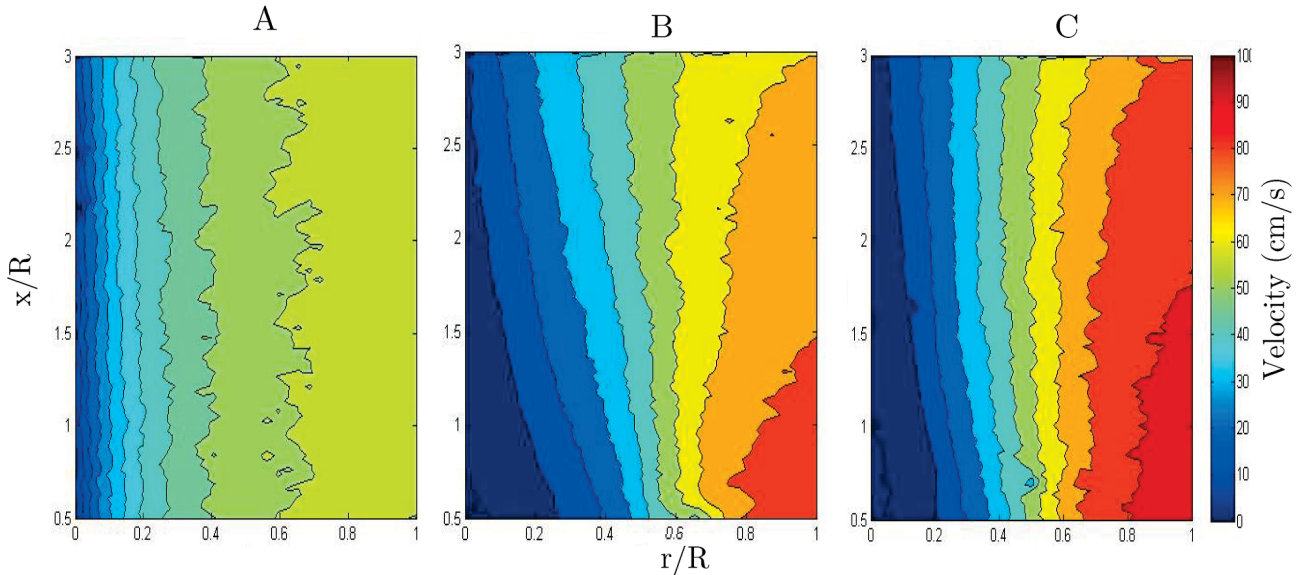


Figure 4-10 - Velocity contour plots from $x/R = 0.5$ to $x/R = 3.0$ for Non-stented flow (A), downstream of a 12 mm (B) and 14 mm (C) stent

The field of view of the camera allowed velocity data to be recorded from the stent exit to 3R. In both full stent cases, flow was not re-established within the FOV (Figure 4-10).

The wall shear stress saw a decrease upon introduction of both stents across the pulse cycle, with the most substantial changes in WSS occurring during acceleration of the fluid (Figure 4-11). Due to the asymmetry in the vessel, the WSS drop varied between the two walls. For comparison, the most severe case is considered. The drop observed at the peak was found to be 82.1% for the 12 mm stent. The 14 mm stent saw a 120.7% in the WSS due to the flow reversal noted at the wall.

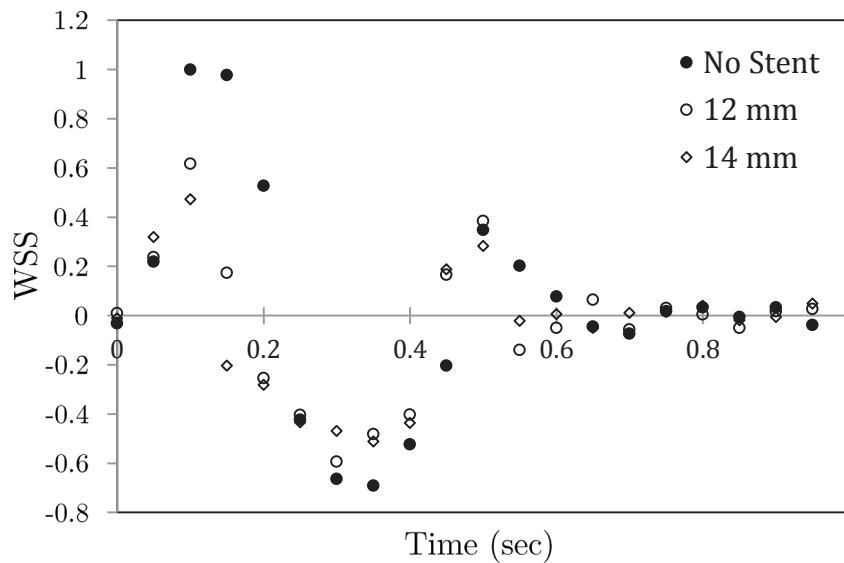


Figure 4-11 - Normalized WSS across the pulse for the 12 mm and 14 mm stent compared to the non-stented flow.

The cycle averaged WSS decreased from 0.920 Pa in the non-stented case to -0.832 Pa and -1.2675 Pa for the 12 mm and 14 mm stent. The change in sign of the cycle averaged WSS indicates a substantial flow reversal over the course of the pulse at the near wall. The OSI, surprisingly, decreased upon stent introduction from 0.4385 to 0.4182 and 0.3642

for the 12mm and 14mm stent, respectively. This is due to the fact that the flow was already pulsatile and therefore highly oscillatory velocities to begin with, which is an important characteristic of flow in the peripheral arteries. The lowering of the WSS in both positive and negative flow direction, led to an overall WSS approaching zero, in turn lowering the OSI.

The turbulence intensity was approximately zero in the acrylic at peak pulse, however it increased upon introduction of the stents (**Figure 4-12**). The 12mm stent caused less flow disturbances, with turbulence intensities as high as one measured along the length of the ROI. The 14mm stent caused much more substantial increases, with the turbulence intensity reaching 5 along the entire ROI length.

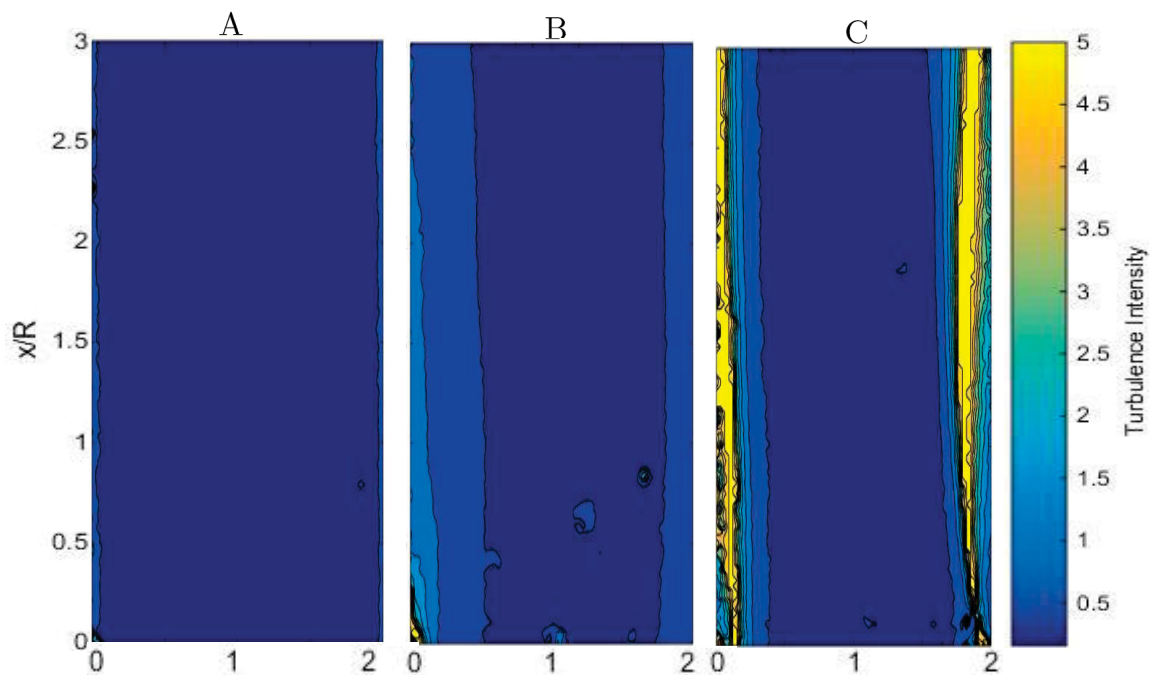


Figure 4-12 - Axial turbulence intensities in non-stented flow (A) and downstream of a 12mm (B) and 14mm (C) Gianturco stent at peak pulse in an acrylic tube.

4.4 Healthy Compliant Vessel

Experiments presented in Section 4.2 were repeated using a Sylgard[®] vessel having a compliance of $7.7 \% \text{ mm Hg}^{-1} \times 10^{-2}$ (C_{Base}), an elasticity representative of a healthy femoral artery [50].

4.4.1 – Individual Stent Wires

Introduction of a single stent wire in the elastic vessel showed similar trends to those observed in the acrylic, however velocity disturbances found were more pronounced. This is to be expected because in addition to the struts encumbering the flow, the fluid is additionally altered due to the wire locally increasing the diameter of the vessel. The wire's presence resulted in a decrease in flow velocities from $0 < r/R = 0.4058$, with the largest absolute change (a 8.77 cm/s decrease) occurring at $r/R = 0.1052$. This was accompanied by an increase in the velocity as high as 11.7% for $0.4058 < r/R < 1$ (Figure 4-13). The WSS was affected by these velocity changes, with a drop at peak pulse of 14.4% at $x/R = 0.5$ from the wire exit (Figure 4-14). The cycle average WSS at that location was found to decrease by 26.9%, while the OSI increased 16.5%.

Upon introduction of a second, and subsequently a third stent wire, no change in flow patterns were observed as compared to the single wire case. Figure 4-15 shows the velocity profile for all three configurations at peak pulse, while Figure 4-16 shows the centerline velocities for the three configurations across the entire one second pulse, demonstrating that no change was identified at any point across the diameter of the stent or anytime time across the pulse cycle. This was also observed in the acrylic measurements.

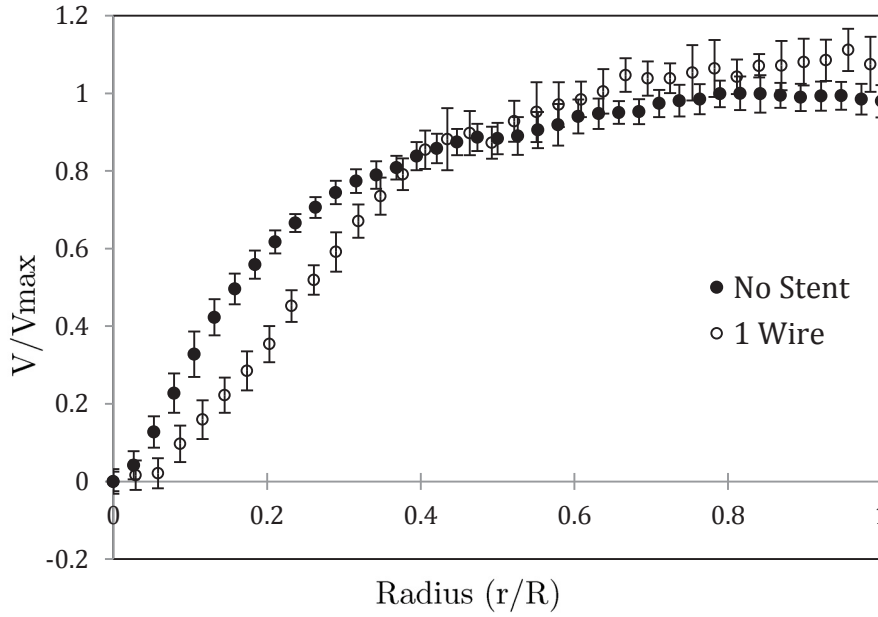


Figure 4-13- Normalized PIV velocity measurements from wall to tube center measured at $x/R = 0.5$ from outlet of a single stent wire compared to non-stented flow in a compliant mock artery (C_{Base}). Error bars represent normalized standard deviations.

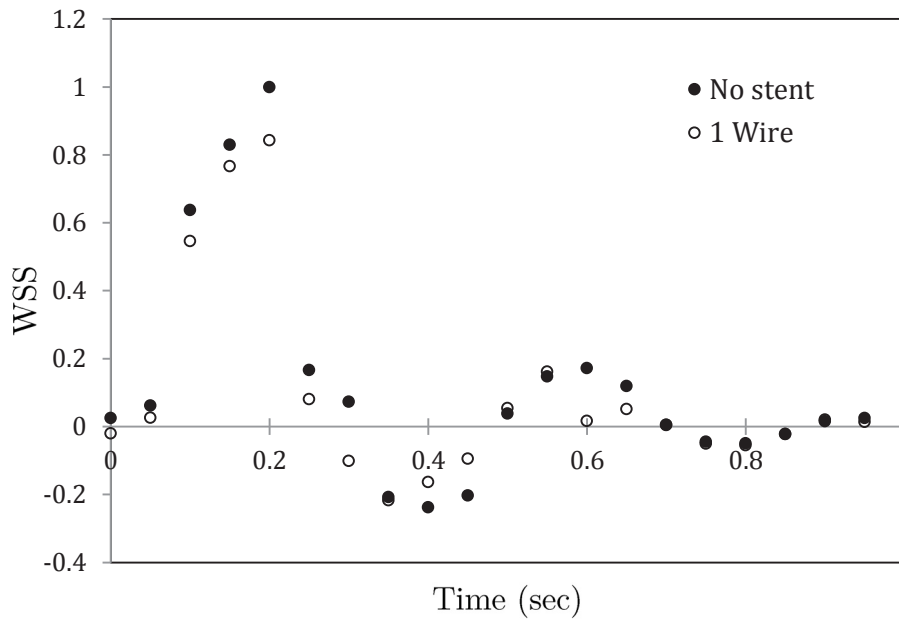


Figure 4-14 - Normalized WSS in single wire stented flow across pulse cycle at $x/R = 0.5$ from stent outlet compared to non-stented flow.

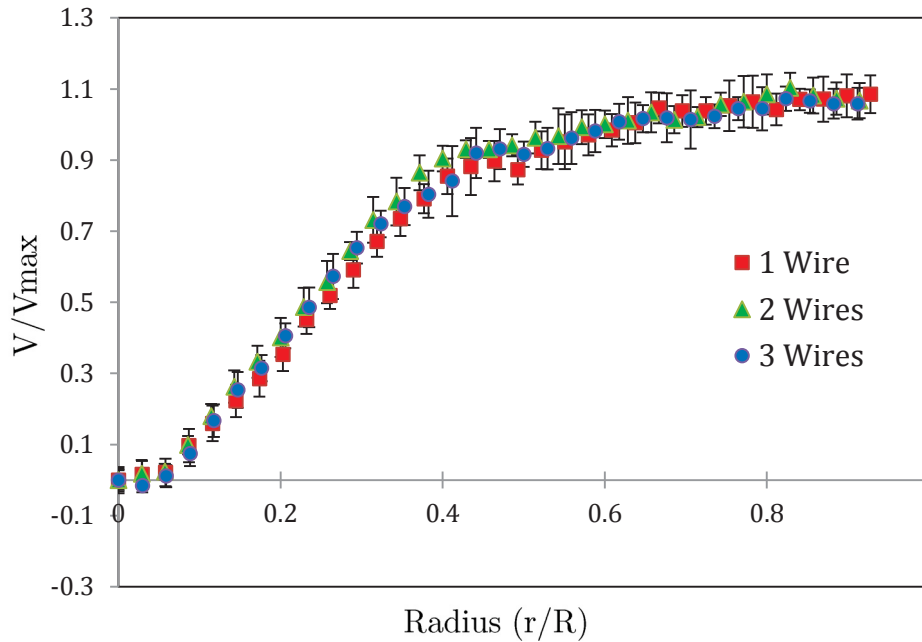


Figure 4-15 - Normalized PIV velocity measurements from wall to tube center measured at $x/R = 0.5$ from outlet of a three stent wire configurations within a compliant mock artery. Error bars represent normalized standard deviations.

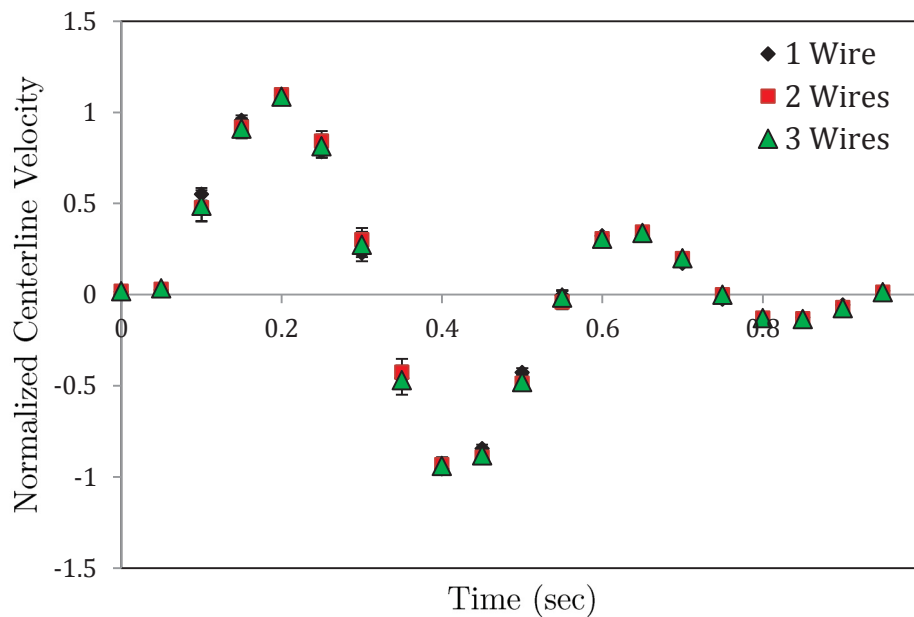


Figure 4-16 - Centerline velocities measured at $x/R=0.5$ from stent exit for one, two, three stent wires. Error bars represent normalized standard deviations.

4.4.2 – Full Stent

Introduction of a full stent produced an initial decrease in velocity at the cross-sections periphery, followed by an accelerated core flow (Figure 4-17), similar to trends observed in the acrylic. For the 12 mm stent, the velocity dropped by as much as 32.2 cm/s (87.4%) between $0 < r/R < 0.6316$ and $1.472 < r/R < 2$. The centerline velocity increased 65.4%. The 14 mm stent caused more severe changes to the peak flow, with a maximum velocity increase of 83.8% (Figure 4-18). The drop in velocity at the outer edge was less pronounced, with a maximum decrease of 18.5 cm/s (63.3 %).

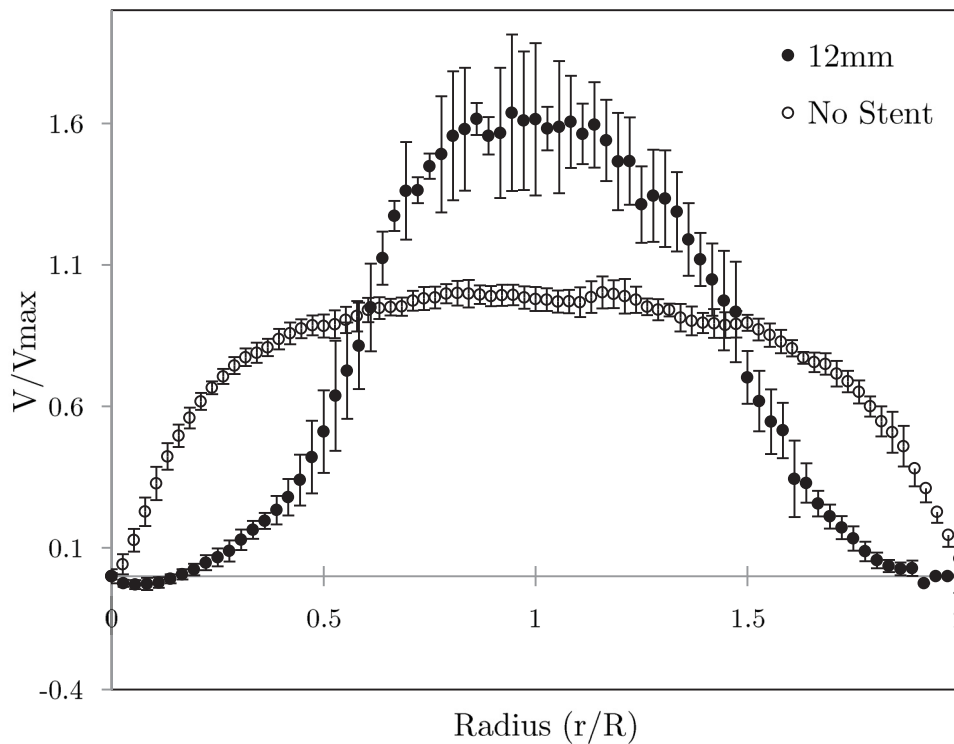


Figure 4-17 - Normalized PIV velocity measurements measured at $x/R = 0.5$ from the stent exit in a compliant mock artery across entire diameter. Error bars represent normalized standard deviations.

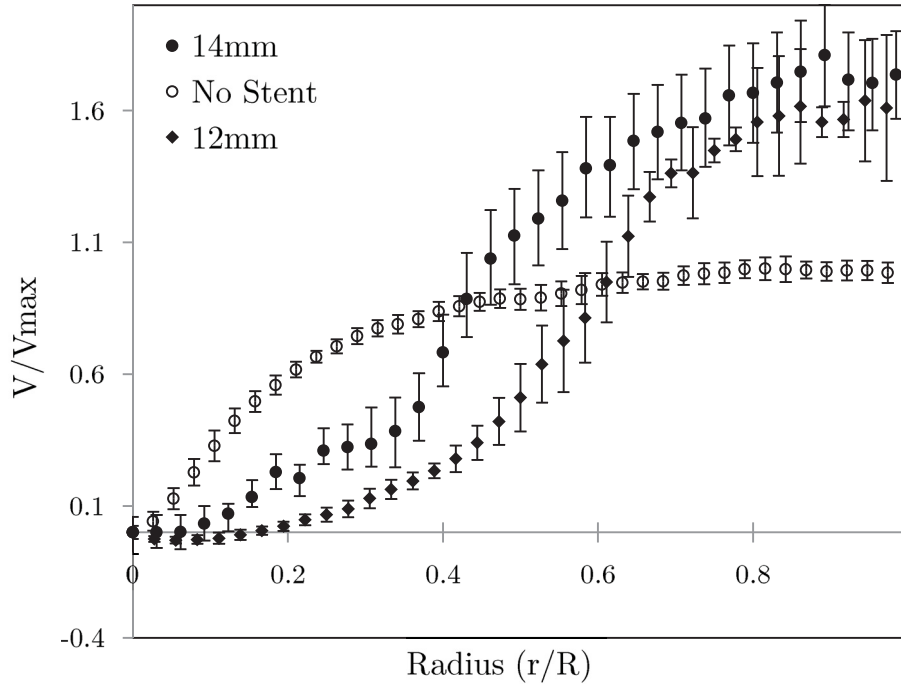


Figure 4-18- Normalized PIV velocity measurements from wall to tube center measured at $x/R = 0.5$ from the stent exit in a compliant mock artery (C_{Base}) for both a 14mm and 12 mm stent. Error bars represent normalized standard deviations.

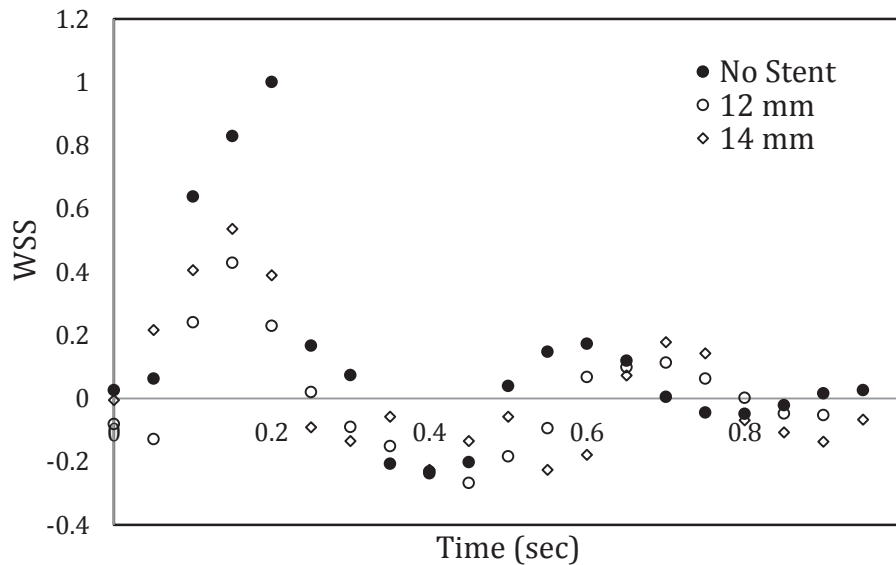


Figure 4-19 - Normalized WSS across pulse cycle at $x/R = 0.5$ from outlet of a 12 mm and 14 mm stent compared to non-stented flow.

The drop in peak WSS was found to be 86.0% in the 12 mm stent and 154.9% in the 14 mm (Figure 4-19). The cycle averaged WSS dropped drastically in both cases, reaching a negative value in the 12 mm case. Introduction of the grafts increased OSI from 0.187 in the non-stented case to 0.477 and 0.435 downstream of the 12 mm and 14 mm stent, respectively.

Turbulence strength was calculate at peak pulse (Figure 4-20). The turbulence strength was highest in the center of the vessel, and increased upon introduction of the stent and was present across the entire ROI. The 14 mm case caused higher turbulence in the center of the vessel, this explains the larger error bars found for the respective velocity profiles.

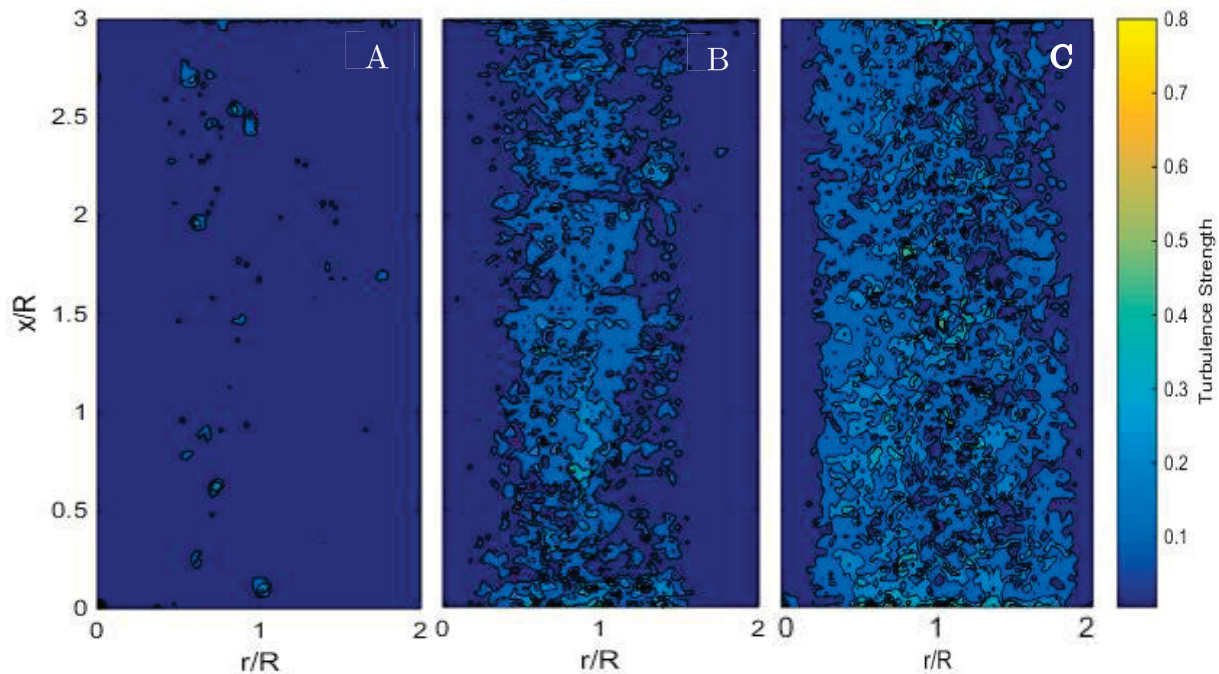


Figure 4-20 - Axial turbulence strengths non-stented flow (A) downstream of a 12 mm (B) 14 mm (C) Gianturco stent at peak pulse in a $7.7 \text{ \% mm Hg}^{-1} \times 10^{-2}$ compliant tube.

4.5 Variable Vessel Compliance

Testing of full stents was repeated using Sylgard® vessels with both a high ($12.92\% \text{ mm Hg}^{-1} \times 10^{-2}$) and a low compliance ($6.2\% \text{ mm Hg}^{-1} \times 10^{-2}$). The general trends were similar to those observed in the acrylic and baseline elastic tubes, with the stents decreasing velocities close to the wall, while increasing centerline velocities. Similar to previous tests, the 14 mm stent showed a larger increase in centerline velocities in both cases compared to the 12 mm. In the case of the low compliance tube the centerline velocities were increased by 43.4% and 76.8% for the 12 mm and 14 mm stent, respectively (Figure 4-21). The largest absolute decreases in velocity occurred at $r/R=0.171$ in both cases and were found to be 16.4 cm/s and 13.9 cm/s.

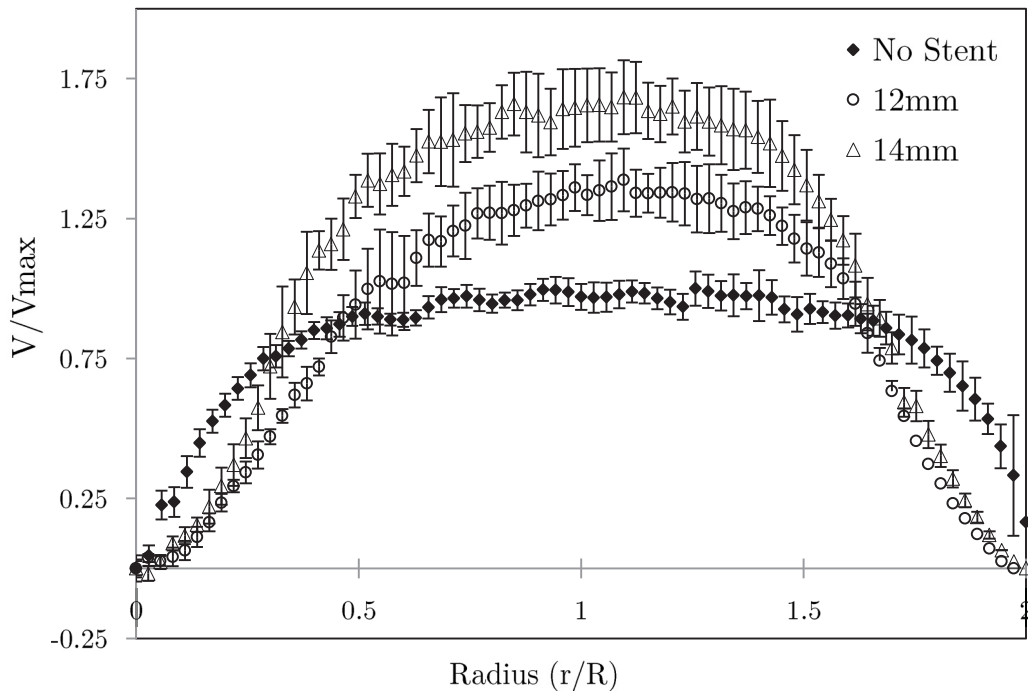


Figure 4-21 - Normalized PIV velocity measurements from wall to wall measured at $x/R = 0.5$ from a stent exit in a compliant mock artery. Error bars represent normalized standard deviations.

The WSS at the peak decreased, with values falling by 84.4% and 43.4% for the 12 mm and 14mm, respectively (Figure 4-23). The cycle averaged WSS decreased from 6.64 Pa to 1.55 Pa and 3.22 Pa, for the two stents. The OSI increased upon introduction of the two stents, from 0.288 in the non-stented vessel to 0.354 and 0.332.

Turbulence intensity, like in the baseline compliant vessel saw minimal change upon stent introduction, while the turbulence strength increased at core flow (Figure 4-22) when a stent was present in the test section.

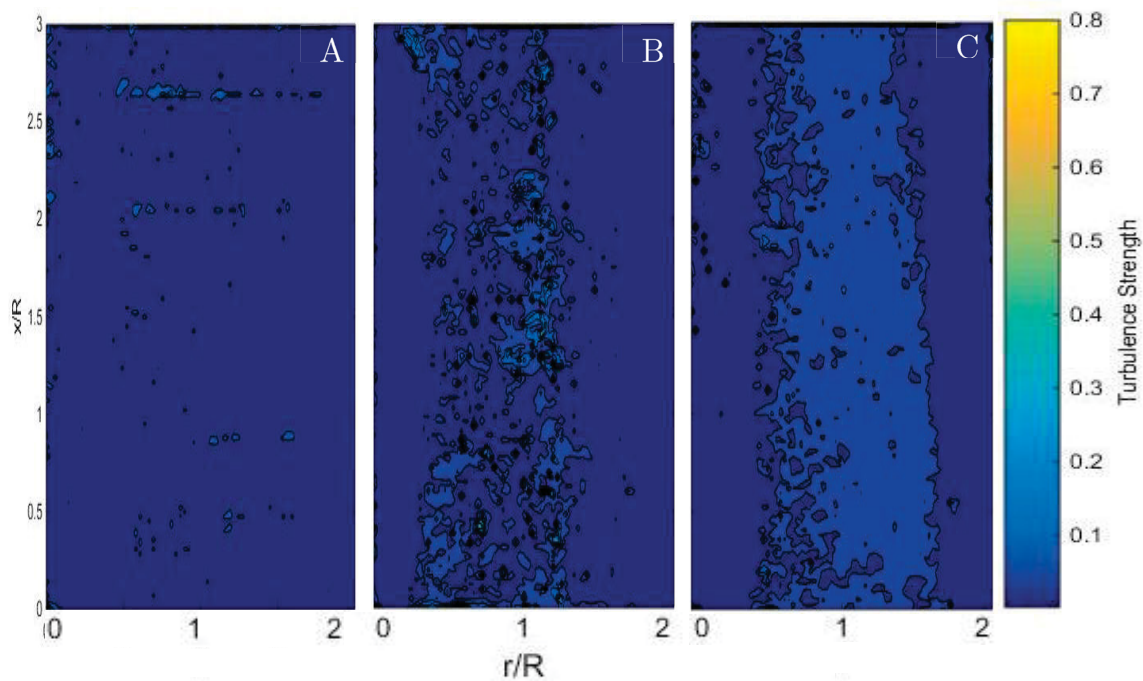


Figure 4-22 - Axial turbulence strengths non-stented flow (A) and downstream of a 12mm (B) and 14mm (C) Gianturco stent at peak pulse in a $6.2 \% \text{ mm Hg}^{-1} \times 10^{-2}$ compliant tube.

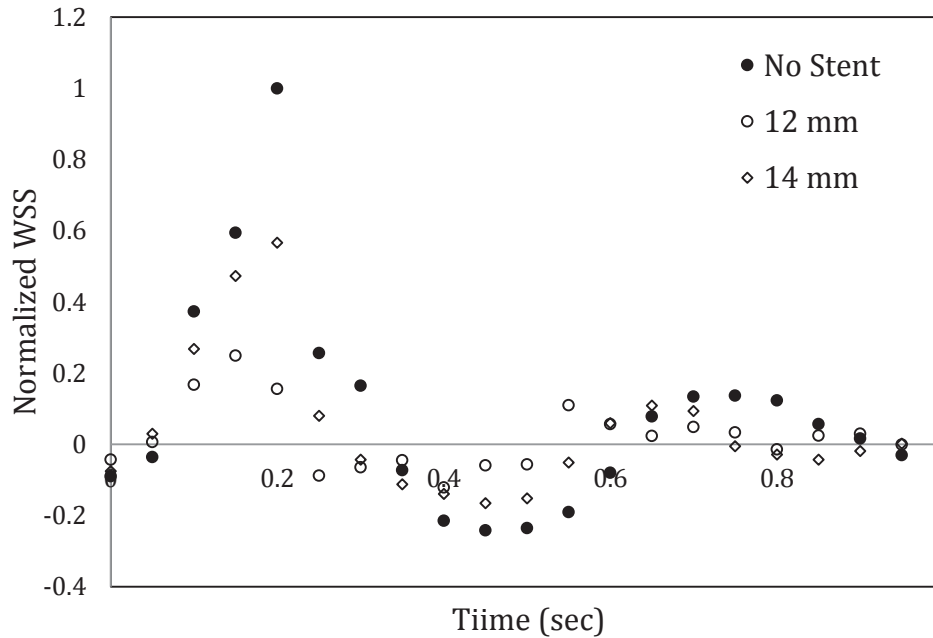


Figure 4-23 - Normalized WSS across pulse cycle at $x/R = 0.5$ from outlet of a 12 mm and 14 mm stent compared to non-stented flow.

In the highly compliant tube, turbulence intensity was greatly increased as demonstrated by the error bars in Figure 4-24, with turbulence strength increasing at core flow upon stent introduction. Despite these fluctuations, the general trends seen in previous tests were still apparent (Figure 4-25). Due to the extreme fluctuations the velocities were difficult to quantify, however at the center of the tube the velocity increased by 41.0% and 51.1% for the 12 mm and 14 mm, respectively. The maximum absolute decrease in velocity for the two stents was found to be 16.9 cm/s and 7.6 cm/s.

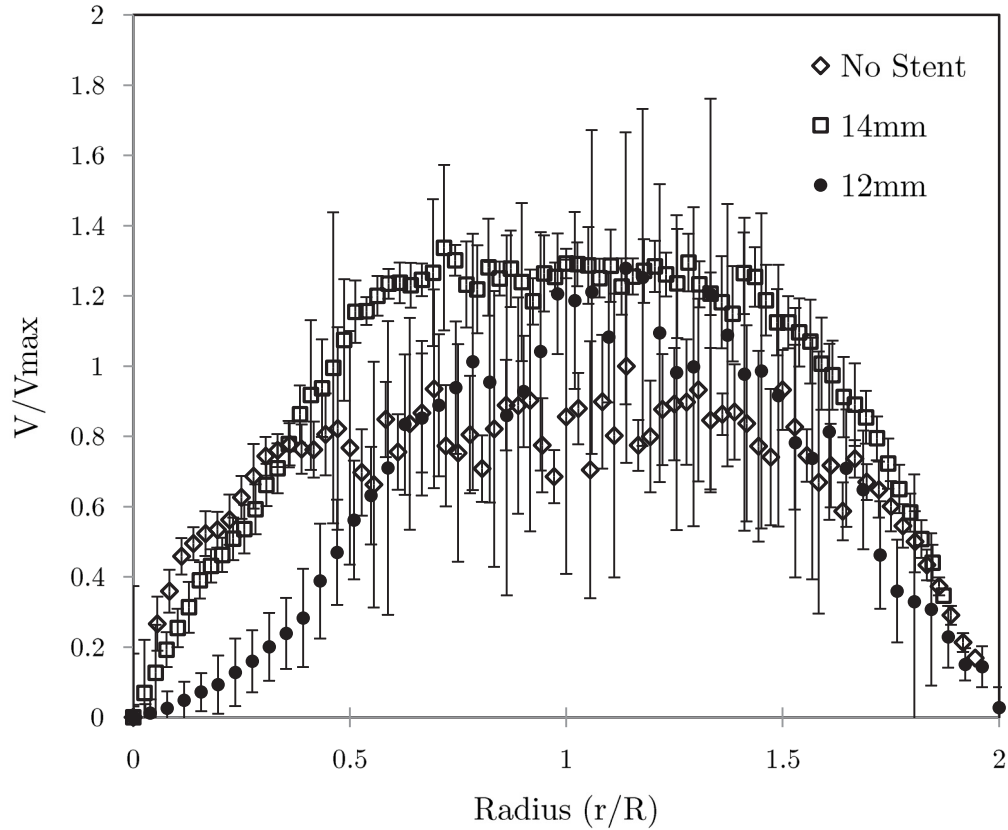


Figure 4-24 - Normalized PIV velocity measurements across tube diameter measured at $x/R = 0.5$ from a stent exit in a compliant mock artery (C_{High}). Error bars represent normalized standard deviations.

The shear stresses were similarly affected in this tube, with a drop in the peak WSS and cycle averaged WSS, accompanied by an increase in the OSI (Figure 4-26). The WSS at peak pulse dropped by 58.3% and 50.72% for the two stents, respectively. The cycle average WSS, initially 7.53 Pa, fell to 4.472 Pa and 5.175 Pa for the 12 mm and 14 mm stent, respectively. Lastly, the OSI increased from 0.214 initially to 0.238 and 0.2509.

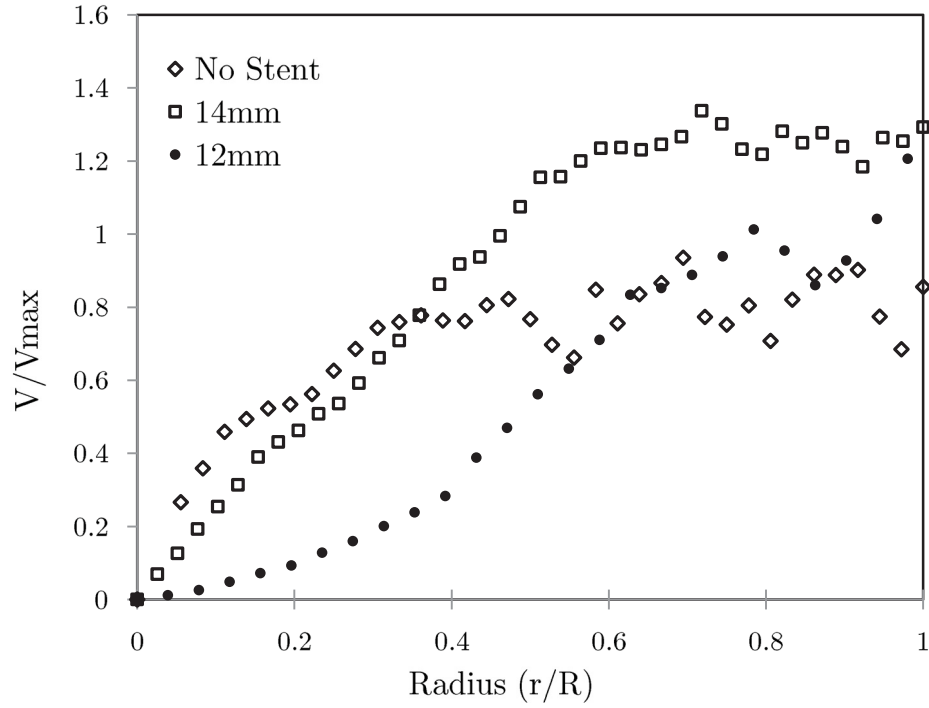


Figure 4-25 - Normalized PIV velocity measurements shown in Figure 4-24, without error bars.

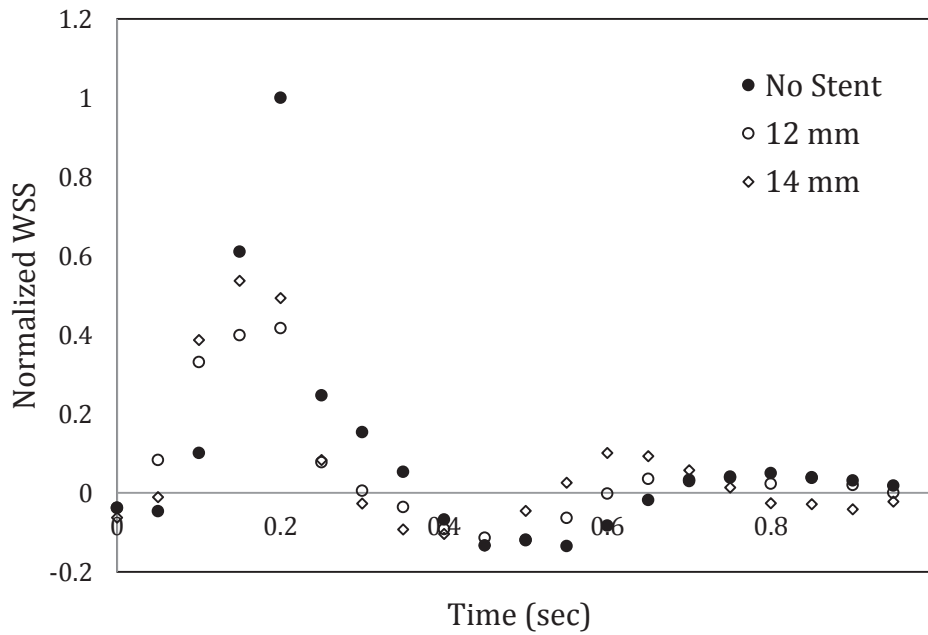


Figure 4-26 - Normalized WSS across pulse cycle at $x/R = 0.5$ from outlet of a 12 mm and 14 mm stent compared to non-stented flow.

Chapter 5 –Discussion

5.1 Implications

5.1.1 Individual Wires

The introduction of a single wire caused only minor flow disturbances in both rigid and compliant vessels, with the effect being more pronounced in the compliant tube. A similar study by Walker [6] in a rigid acrylic tube (6.35 mm ID) and using Z-wires showed more substantial effects after wire placement, particularly on the WSS alterations [6]. Centerline velocity increases were reported between 12-18%, which are slightly higher than those observed here (4.65% and 11.7% in the acrylic and Sylgard, respectively). The velocity close to the wall, however, showed much larger drops in [6], decreasing the WSS drastically (almost to zero), whereas only minor changes were noted in this study (22% at peak pulse). The smaller vessel diameter could account for this difference as the area of wire exposed to the flow compared to cross-sectional area of the tube is much lower in the present study. Additionally, the smaller tube was representative of an arterial segment that did not have reverse flow and therefore all negative axial flow was due to stent placement. This meant that any drop in the WSS would cause the OSI to increase, whereas in the case of an initially oscillatory flow, changes to the WSS could increase or decrease the OSI, depending on the magnitude and direction of the change.

The introduction of subsequent stent wires had no effect on the flow downstream in either compliant or rigid tubes. This was observed at every time point across the pulse and for every cross-sectional location downstream of the stent. This is most likely due to the fact that the bare wires only caused disturbances close to the wire outlet. Wires were 1.5 cm

long and 0.4 cm apart (the intra-wire distance in full jacketed stents), allowing the flow enough space to recover before reaching subsequent wires.

5.1.2 Effect of Stent Cover

The impact of adding the covered stent as compared to the three bare wires was substantial, with the velocity profile changing drastically as well as introducing asymmetry and inconsistencies. These inconsistencies were more pronounced in the 12 mm stent, due to it having less wire peaks, decreasing the spatial coverage of the wires at the wall and allowing the stent and fabric to deploy with some additional protrusions.

Centerline velocity increases jumped from 4.65% in the 3 wire case to 65.4% for the fully covered stent. Additionally the largest absolute drop in velocity grew from 5.31 cm/s in the bare wire case to 35.6 cm/s with the same three wires in a covered stent. Associated WSS and turbulence strengths saw similar deviations, with the fully covered stent causing substantially more variations. In the acrylic tube, the cycle averaged WSS fell from 0.9477 Pa in the bare wire case to -0.8320 Pa and -1.268 Pa for the 12 mm and 14 mm stent, respectively.

With no cover the flow recovered within one radius from the stent exit, however in the case of the full stent the flow was severely altered for the entire length of the FOV. This is in agreement with observation reported by Greil et al., of the carotid bifurcation using a MembraX stent [42]. It was shown that introduction of the fabric covering substantially increased centerline slipstreams as compared to the same uncovered wires, as well as increasing the length required for flow to recover from 4 mm in the uncovered case to 10 mm with a covered stent.

Additionally, Greil et al. [37] collected measurements for a modified MembraX stent, in which the fabric covering was cut such that the bare wires extended out of the fabric at the entrance and exit of the stent. This increased the membranes contact with the vessel wall and was shown to completely eliminate flow separation that had been observed distally from the unmodified stent. This supports our observation that the increase in spatial coverage provided by the 14 mm stent wires decreased perturbances at the wall compared to the 12 mm stent.

Protocols were established to ensure stents deployed reliably for each test and markers were used to confirm the wires were aligned consistently for all runs, something which cannot be guaranteed in vivo. The stent was inserted such that there was no twisting between each subsequent stent wire, however should the stent deploy with some tortuosity, a narrowing will occur in the fabric between the two wires which severely hinders the blood flow. This was observed in a preliminary test where some twisting occurred between subsequent wires and the flow was almost entirely obstructed in a section of the tube.

5.1.3 Effect of Oversizing and Compliance Mismatch

The compliance change of the host vessel had several important implications on the flow parameters both before and after stent deployment. Compared to the acrylic test section, the Sylgard® vessels had a capacitance effect, storing a volume of fluid with each pulse and thereby slightly decreasing the instantaneous flowrate at the peak. Furthermore, the flow was less predictable at higher compliances as demonstrated by the increasing turbulence intensities, particularly at the center of the tube.

Both the 20% and 40% oversizing consistently reduced velocities at the vessel peripheries while increasing centerline velocities. While the 20% oversizing created a larger drop at the vessel periphery, the 40% oversizing caused larger increases in centerline velocities at peak flow. This trend was apparent for tests run in both acrylic and Sylgard® vessels. The centerline velocity increase caused by the 14 mm stent was 10.1%-33.4% larger than increases caused by the 12 mm stent (with the lowest and highest difference being a result of the most and least compliant tube, respectively). Interestingly, the effect of oversizing appears to be interrelated to the compliance of the vessel- the more rigid the tube the less ability to stent has to expand once deployed. The largest difference in peak centerline velocities for the two stents occurred in the most rigid Sylgard® vessel, due in part to the vessel's rigidity holding the stent in a semi-folded position. This is due to the larger 14 mm stent being compressed inside the same diameter tube, without much change to the host vessel's diameter. From PIV images the unpressurized expansion in the tube due to the introduction of the stent could be measured. On average, the 14 mm stent expanded the ID of the vessel only 0.114 mm more than the 12 mm (across all tube compliances) - a small increase considering the nominal diameter was 2 mm larger. Moreover, the difference in expansion between the two sizes varied only slightly across compliances.

A study by Johnston et al. found that smaller sized Gianturco stents produce greater radial forces than larger stents, while that force increases with increasing diametric constriction [52]. Therefore it would be reasonable to assume that a 12 mm stent compressed 16.7% diametrically could result in a comparable radial force to that generated by a 14 mm stent compressed 40% diametrically. As such, once expanded in the test section the actual diameter of the vessel was only slightly larger for the 14 mm, despite

having an additional wire peak and being 2 mm larger in diameter (6.3 mm bigger circumferentially). This additional material was compressed inside the test section, resulting in larger disturbances centrally and overall higher velocities. Peripherally, however, the 12 mm stent had a more pronounced impact on the flow parameters, due to it having overall lower velocities than the 14 mm stent. This caused the absolute drops in the velocity to be larger and consequently larger decreases in the cycle averaged WSS were observed.

In the Sylgard vessels the introduction of stents decreased WSS and increased OSI compared to their respective non-stented case, however no clear trend was discernible as to the effect of the compliance. The largest change to the WSS was observed in the mid-compliance vessel, which complicated determining a clear effect of the compliance mismatch.

5.2 Limitations

Although every effort was made to replicate in-vivo parameters, the main limitations in this study are due to the difficulty in quantifying and characterizing physiological parameters, particularly arterial compliance and blood flow features. Bulk compliance was closely matched using the Sylgard®, however in-vivo conditions encompass vaso-dilation and constriction, geometric inconsistencies such as plaque accumulations and calcifications, upsurges in stiffness as the vessel expands, as well as variations across ages, genders and disease state. Additionally, endografts are often deployed in vessels of increased diameter and decreased wall thickness due to disease, which was neglected.

The FOV was limited to three radii from the stent exit, with flow within the stent completely inaccessible due to the stent covering. Re-stenosis has been shown to occur most frequently within and immediately downstream of the vessel, therefore measurements inside of the stent could be valuable. Additionally, for full stents the flow did not recover within the FOV, therefore conclusions drawn as to the length of vasculature which would be affected by flow disturbances would be speculative.

Lastly, the calculations of the WSS found the strain rate using only the first vector row and assuming zero flow at the wall. The error in velocity measurements was lowest close to the wall, making this point reliable across a data collections run, however any slight deviations in this value could have huge ramifications in final calculated WSS. This is due to the fact that the strain rate found is not only proportional to the WSS (as shown in equation 3.7), but is also used to find the local instantaneous viscosity (using the Carreau-Yasuda estimation) which is directly proportional to the WSS calculated. Although this is a common method for inferring WSS from velocity measurements, particularly in LDA and PIV applications [53], its reliance on a single point was not ideal. This was further complicated in the Sylgard vessel where the continuous motion of the wall required the first vector row to be identified for each image frame, which was done manually. In the event that the vessel edge was not selected accurately the calculation of the WSS, being reliant on that single value, could introduce error.

Chapter 6 – Conclusions and Recommendations

6.1 Summary and Conclusion

To conclude, the parameters downstream of Gianturco stent graft wires and two sizes of full jacketed stents were quantified. The effect of implanting a single wire was shown to cause slight changes to parameters, while adding additional wires had no effect on the flow downstream. This was attributed to the small distance required for these perturbations to return to normal conditions. The addition of a stent with a fabric sheath, however, had important ramifications on hemodynamic parameters which are known to affect the long term patency of stents, such as WSS and OSI. Furthermore, these changes extend far passed the stent exit.

For all test configurations the centerline velocities were increased compared to non-stented flows and velocities at the wall decreased (with negative flows present in some cases). These effects caused decreases to the cycle averaged WSS for all cases compared to the respective non-stented case. Interestingly, the OSI decreased upon introduction of the stents due to the already oscillatory nature of the pulse in the non-stented flow. Changes to these fluid parameters are associated with stent failure, with areas of high moving flow leading to platelet activation and associated thrombosis, while areas of slow and reversing flow shown to be atherogenic. Furthermore, changes to the flow will prompt vascular remodeling and subsequent narrowing of the lumen.

The global effect of the compliance mismatch and oversizing is complex and multifactorial, requiring further investigation. However, our observations suggest that the compliance of

the vessel impacts the incomplete expansion of the stent, with only a slight increase in diameter with more oversizing observed.

These findings imply the following conclusions;

- Implantation of a single wire causes minimal fluid disturbances in a larger tube.
- The addition of subsequent stent wires has no discernable effect on the flow.
- Addition of the fabric sheath increases flow disturbances as compared to bare wires.
- More oversizing does not increase the flow area despite the presence of a larger stent, causing a greater constriction. Consequently, centerline velocities are increased with increasing oversizing.
- The combined disturbance caused by compliance mismatch and oversizing cannot be easily separated into two component effects as the compliance directly affects the stents ability to expand to its nominal diameter, which is also dependent on the degree of oversizing. However, based on these observations we can posit that oversizing is more detrimental to the normal flow of blood than the compliance mismatch.

6.3 Future Work and Recommendations

The results obtained lay the groundwork for further investigation into compliance mismatch and stent sizing. Although differences were noted between varying compliance of vessels, the specific impact of these changes remains unclear, warranting further examination. Using the method established in this work more vessel compliances, having finer resolution, could easily be made and flow parameters quantified. Further investigation could aid in better defining best practices for stent selection.

Furthermore, the vessel geometry, both in compliant and acrylic vessels could be made to include an aneurysmal bulge. This could be easily achieved using current molding techniques. Using the PIV set-up flow could be quantified for varying degrees of radial dilation severity. As endoleaks are the primary reason for secondary interventions, investigations could examine various stent deployment positions and explore flow properties and leaking for several stent positions [13]. Most interesting would be the current set-up's ability to image flow within the aneurysmal sac, directly outside the stent-graft.

References

- [1] M. Desai, J. Eaton-Evans, C. Hillery, R. Bakhshi, Z. You, J. Lu, G. Hamilton and A. Seifalian, "AAA Stent-Grafts: Past Problems and Future Prospects," *Annals of Biomedical Engineering* , vol. 38, no. 4, pp. 1259-1275, April 2010.
- [2] J. S. Coselli, S. Y. Green and S. A. LeMaire, "When Stent-Grafts Fail: Extraction and Open Surgical Repair of the Thoracic Aorta," *Texas Heart Institute Journal*, vol. 38, no. 6, p. 658–660, 2011.
- [3] R. Greenhalgh, "Comparison of endovascular aneurysm repair with open repair in patients with abdominal aortic aneurysm (EVAR trial 1), 30-day operative mortality results: randomised controlled trial.," *The Lancet* , vol. 364, no. 9437 , pp. 843-848, 2004.
- [4] J. De Bruin, A. F. B. Baas, J. Buth, M. Prinssen, E. L. Verhoeven, P. W. Cuypers, M. R. v. S. van Sambeek and R. Balm, "Long-Term Outcome of Open or Endovascular Repair of Abdominal Aortic Aneurysm," *The New England Journal of Medicine* , vol. 362, no. 20, pp. 1881-1889, 2010.
- [5] J.-J. Chiu and S. Chien, "Effects of Disturbed Flow on Vascular Endothelium: Pathophysiological Basis and Clinical Perspectives," *Physiological Reviews*, vol. 91, no. 1, p. 327–387, 2011.
- [6] A. Walker, *The Characterization of Common Cardiovascular Flow Regimes Using Newtonian and Non-Newtonian Fluids*, U. o. Calgary, Ed., Calgary, Alberta: Department of Mechanical Engineering , 2013.
- [7] N. Duraiswamy, R. T. Schoepfoerster, M. R. Moreno and J. E. Moore, "Stented Artery Flow Patterns and Their Effects on the Arterial Wall," *Annual Review of Fluid Mechanics* , vol. 39, pp. 357-382, 2007.

- [8] D. Stoeckel, C. Bonsignore and S. Duda, "A Survey of Stent Designs," *Min Invas Ther & Allied Technol*, vol. 11, no. 4, pp. 137-147, 2002.
- [9] S. Chien, "Mechanotransduction and endothelial cell homeostasis: the wisdom of the cell," *American Journal of Physiology*, vol. 292, no. 3, pp. H1209-H1224, 2007.
- [10] H. Y. Chen, J. Hermiller, A. K. Sinha, M. Sturek, L. Zhu and G. S. Kassab, "Effects of stent sizing on endothelial and vessel wall stress: potential mechanisms for in-stent restenosis," *Journal of Applied Physiology*, p. 1686-1691, 2009.
- [11] B. M. Jackson and J. P. Carpenter, "Devices Used for Endovascular Aneurysm Repair: Past, Present, and Future," *Seminars in Interventional Radiology*, vol. 26, no. 1, pp. 39-43, 2009.
- [12] J. van Prehn, F. Schlosser, B. Muhs, H. Verhagen, F. Moll and J. van Herwaarden, "Oversizing of Aortic Stent Grafts for Abdominal Aneurysm Repair: A Systematic Review of the Benefits and Risks," *Eur J Vasc Endovasc Surg*, pp. 42-53, 2009.
- [13] G. Schurink, N. Aarts and J. van Bockel, "Endoleak after stent-graft treatment of abdominal aortic aneurysm: a meta-analysis of clinical studies," *British Journal of Surgery*, 1999.
- [14] A. Schanzer, R. K. Greenberg, N. Hevelone, M. William P. Robinson, M. H. Eslami, R. J. Goldberg and L. Messina, "Predictors of Abdominal Aortic Aneurysm Sac Enlargement After Endovascular Repair," *Circulation*, vol. 123, pp. 2848-2855, 2011.
- [15] D. M. Wootton and N. D. Ku, "Fluid Mechanics of Vascular Systems, Diseases and Thrombosis," *Annual Review of Biomedical Engineering*, vol. 1, pp. 299-329, 1999.

- [16] C. Jeng-Jiann and S. Chien, "Effects of Disturbed Flow on Vascular Endothelium: Pathophysiological Basis and Clinical Perspectives," *Physiological Reviews*, vol. 91, no. 1, pp. 327-387, 2011.
- [17] C. Hahn and M. Schwartz , "Mechanotransduction in vascular physiology and atherogenesis," *Nat Rev Mol Cell Biol*, vol. 10, no. 1, pp. 53-62, 2009.
- [18] M. S. Kim and L. S. Dean, "In-Stent Restenosis," *Cardiovascular Therapeutics*, vol. 29, no. 3, pp. 190-198, 2011.
- [19] E. R. Edelman and C. Rogers, "Pathobiologic Responses to Stenting," *The American Journal of Cardiology*, vol. 81, pp. 4A-6A, 1998.
- [20] B. Langille and F. O'Donnell, "Reductions in arterial diameter produced by chronic decreases in blood flow are endothelium-dependent," *Science*, vol. 231, no. 4736, pp. 405-407 , 1986.
- [21] J. Dzau and G. H. Gibbons, "Vascular Remodeling: Mechanisms and Implications," *Journal of Cardiovascular Pharmacology*, vol. 21, no. Suppl.1, pp. S1-S5, 1993.
- [22] A. M. Melkumyants, S. A. Balashov, Khayutin and V. M., "Endothelium dependent control of arterial diameter by blood viscosity," *Cardiovascular Research*, vol. 23, no. 9, pp. 741-747, 1989.
- [23] I. Di Stefano, D. Koopmans and B. Langille, "Modulation of arterial growth of the rabbit carotid artery associated with experimental elevation of blood flow," *Journal of Vascular Research*, vol. 35, no. 1, pp. 1-7, 1998.
- [24] A. M. Shaaban and A. J. Duerinckx, "Wall Shear Stress and Early Atherosclerosis: A Review," *The American Journal of Roentgenology*, vol. 174, no. 6, pp. 1657-1666, 2000.

- [25] K. S. Cunningham and A. Gotlieb, "The role of shear stress in the pathogenesis of atherosclerosis," *Laboratory Investigation*, vol. 85, no. 1, pp. 9-23, 2005.
- [26] S. Nomura, N. N. Tandon, . T. Nakamura and J. Cone, "High-shear-stress-induced activation of platelets and microparticles enhances expression of cell adhesion molecules in THP-1 and endothelial cells," *Atherosclerosis* , vol. 158, no. 2, pp. 277-287, 2001.
- [27] Y. Miyazaki, S. Nomura, T. Miyake, H. Kagawa and C. Kitada, "High Shear Stress Can Initiate Both Platelet Aggregation and Shedding of Procoagulant Containing Microparticles," *Blood Journal* , vol. 88, no. 9, 1996.
- [28] W. M. Abbott, J. Megerman, J. E. Hasson, . G. L'Italien and D. F. Warnock, "Effect of compliance mismatch on vascular graft patency," *Journal of Vascular Surgery*, vol. 5, no. 2, p. 376–382, 1987.
- [29] C. Kinley and A. Marble, "Compliance: a continuing problem with vascular grafts.," *The Journal of cardiovascular surgery*, vol. 21, no. 2, 1980.
- [30] H. Alderson and M. Zamir , "Effects of Stent Stiffness on Local Hemodynamics with Particular Reference to Wave Reflections," *Journal of Biomechanics* , vol. 37, pp. 339-348, 2004.
- [31] J. L. Berry, E. Manoach, C. Mekkaoui, P. H. Rolland, J. Moore and A. Rachev, "Hemodynamics and Wall Mechanics of a Compliance Matching Stent: In Vitro and In Vivo Analysis," *Journal of Vascular Interventional Radiology*, vol. 13, pp. 97-105, 2002.
- [32] N. Selvarasu, . D. K. Tafti and P. P. Vlachos, "Hydrodynamic Effects of Compliance Mismatch in Stented Arteries," *Journal of Biomechanical Engineering* , vol. 133, no. 2, 2011.

- [33] A. Tortoriello and A. Pedrizzetti, "Flow-tissue Interaction with Compliance Mismatch in a Model Stented Artery," *Journal of Biomechanics* , vol. 37, pp. 1-11, 2004.
- [34] F. Gijsen, F. van de Vosse and J. Janssen , "The Influence of the non-Newtonian Properties of Blood on the Flow in Large Arteries: Steady Flow in a Carotid Bifurcation Model," *Journal of Biomechanics*, vol. 32, pp. 601-608, 1999.
- [35] S. Natarajan and M. Mokhtarzadeh-Dehghan, "A Numerical and Experimental Study of Periodic Flow in a Model of a Corrugated Vessel with Application to Stented Arteries," *Medical Engineering & Physics* , vol. 22, pp. 555-566, 2000.
- [36] J. Peacock, S. Hankins, T. Jones and R. Lutz, "Flow Instabilities Induced by Coronary Artery Stents : Assessment with an In Vitro Pulse Duplicator," *Journal of Biomechanics*, vol. 28, no. 1, pp. 17-26, 1995.
- [37] O. Greil, . G. Pflugbeil, K. Weigand and W. Weiß, "Changes in Carotid Artery Flow Velocities After Stent Implantation: A Fluid Dynamics Study With Laser Doppler Anemometry," *Journal of Endovascular Therapy*, vol. 10, pp. 275-284, 2003.
- [38] J. Chankro, S. Karri, J. Schmieg, S. Prabhu and P. Vlachos, "In Vitro Comparison of the Effect of Stent Configuration on Wall Shear Stress Using Particle Image Velocimetry," *Annals of Biomedical Engineering* , vol. 38, no. 3, pp. 889-902, 2010.
- [39] S. K. Yazdani, E. J. Moore , L. J. Berry and P. P. Vlachos , "DPIV Measurements of Flow Disturbances in Stented Artery Models: Adverse affects of Compliance Mismatch," *Journal of Biomedical Engineering* , vol. 126, pp. 559-566, 2004.
- [40] L. Morris, F. Stefanov and T. McGloughlin, "Stent graft performance in the treatment of abdominal aortic," *Journal of Biomechanics*, vol. 46, pp. 383-395, 2013.

- [41] J. F. LaDisa, I. Guler, E. L. Olson, A. D. Hettrick, R. J. Kerstein, D. C. Warltier and P. S. Pagel, "Three-Dimensional Computational Fluid Dynamics Modeling of Alterations in Coronary Wall Shear Stress Produced by Stent Implantation," *Annals of Biomedical Engineering* , vol. 31, pp. 972-980, 2003.
- [42] O. Greil, T. Kleinschmidt, W. Weiss, O. Wolf, P. Heider, S. Schaffner, M. Gianotti, T. Schmid, D. Liepsch and H. Berger, "Flow Velocities After Carotid Artery Stenting: Impact of Stent Design. A Fluid Dynamics Study in a Carotid Artery Model with Laser Doppler Anemometry.," *Journal of Cardiovascular Interventional Radiology* , vol. 28, pp. 66-76, 2005.
- [43] P. Lewis, J. V. Psaila, R. H. Morgan, W. T. Davies and J. P. Woodcock, "Common femoral artery volume flow in peripheral vascular disease," *Issue British Journal of Surgery*, vol. 77, no. 2, p. 183–187, 2005.
- [44] C. Brake, *Design of a Cardiovascular Flow Mimicking Pump*, Halifax, NS: Department of Mechanical Engineering, Dalhousie University, 2015.
- [45] K. Brookshields and J. Tarbell, "Evaluation of a Transparent Blood Analog Fluid: Aqueous Xanthan Gum/Glycerin," *Bioreheology*, vol. 30, pp. 107-116, 1994.
- [46] D. N. Ku, "Blood Flow in Arteries," *Annual Review of Fluid Mechanics*, vol. 29, pp. 399-434, 1997.
- [47] A. Fronek, M. Coel and E. Bernstein, "Quantitative Ultrasonographic Studies of Lower Extremity Flow Velocities in Health and Disease," *Circulation*, vol. 53, no. 6, pp. 957-960, 1976.
- [48] C. Caro, *The Mechanics of the Circulation*, Cambridge University Press, 2012.

- [49] J. D. Bronzino, *The Biomedical Engineering Handbook : Volume 1 of The electrical engineering handbook series*, Springer Science & Business Media, 2000.
- [50] N. R. M. Tai, A. Giudiceandrea, H. J. Salacinski, A. M. Seifalian and G. Hamilton, "In vivo femoropopliteal arterial wall compliance in subjects with and without lower limb vascular disease," *Journal of Vascular Surgery*, vol. 30, no. 5, p. 936–945, 1999.
- [51] W. Thielicke and E. Stamhuis, "PIVlab - Towards User-friendly, Affordable and Accurate Digital Particle Image Velocimetry in MATLAB," *Journal of Open Research Software*, vol. 2, no. 1, p. e30, 2014.
- [52] C. R. Johnston, K. Lee and J. Flewitt, "The Mechanical Properties of Endovascular Stents: An In Vitro Assessment," *Journal of Cardiovascular Engineering*, vol. 10, no. 3, pp. 128-135, 2010.
- [53] P. Hochareon, K. B. Manning and A. A. Fontaine, "Wall Shear-Rate Estimation Within the 50cc Penn State Artificial Heart Using Particle Image Velocimetry," *Journal of Biomechanical Engineering*, vol. 126, no. 4, pp. 430-437, 2004.
- [54] A. Carroccio, P. L. Faries, N. J. Morrissey, V. Teodorescu, J. A. Burks, E. C. Gravereaux, L. H. Hollier and M. L. Marin, "Predicting iliac limb occlusions after bifurcated aortic stent grafting: Anatomic and device-related causes," *Journal of Vascular Surgery*, 2002.
- [55] H. Samady, . P. Eshtehardi, M. C. McDaniel, J. Suo, S. S. Dhawan, C. Maynard, L. H. Timmins and A. A. Quyyumi, "Coronary Artery Wall Shear Stress Is Associated With Progression and Transformation of Atherosclerotic Plaque and Arterial Remodeling in Patients With Coronary Artery Disease," *Circulation*, vol. 124, no. 7, pp. 779-788, 2011.

- [56] J. L. Berry, A. Santamarina, J. Moore, S. Roychowdhury and W. Routh, "Experimental and Computational Flow Evaluation of Coronary Stents," *Annals of Biomedical Engineering* , vol. 28, pp. 386-398, 2000.
- [57] David M. Wootton and D. N. Ku, "Fluid Mechanics of Vascular Systems, Diseases and Thrombosis," *Annual Review of Biomedical Engineering* , pp. 299-329, 1999.
- [58] F. Nicoud, H. Vernhet and M. Dauzat, "A Numerical Assessment of Wall Shear Stress Changes After Endovascular Stenting," *Journal of Biomechanics* , vol. 38, pp. 2019-2027, 2005.

Appendix A- Results Matlab Code

Vector Field Averages

```
clear all

% Path to Open File for Images
OpenPath = uigetdir('C:\', 'Select folder containing input JPEG files:');
if OpenPath == 0 % This loop will exit the code if the user does not select a
folder
    return
end

for i = 1:400
    OpenName = sprintf('%04d', i);
    infile = [OpenPath '\Raw Velocity Profiles\PIVlab_' OpenName '.txt'];
    data = csvread(infile,4,0);
    data_all(:, :, i)=data(:, :);
end

%To access a specific file, and/or specific data within a file:
%datapoints = data_all[row#,column#,frame#]

%Divide the data into 20 separate pulses
for i=1:20
    for j=1:20
        rearrange(:, :, i, j)=data_all(:, :, j+(20*(i-1)));
        stddevmat(:, i, j)=rearrange(:, 4, i, j);
    end
end

%rearrange(vector row, vector column(x,y,u,v), which pulse, point in pulse)

%Every other pulse
for i=1:10
    r1(:, :, i, :)=rearrange(:, :, 2*i-1, :);
    r2(:, :, i, :)=rearrange(:, :, (2*i-1)+1, :);
    sd1(:, i, :)=stddevmat(:, 2*i-1, :);
    sd2(:, i, :)=stddevmat(:, (2*i-1)+1, :);
end

%Average each pulse
V1=mean(r1, 3);
V2=mean(r2, 3);
std1=std(sd1, 1, 2);
std2=std(sd2, 1, 2);
```

Volumetric Flowrate

```
y=100; %y is the distance from the stent
D=1 %[centimeters]
x=0 %Number of vectors to exclude at the edge if any

for i=1:20
    file= sprintf('AvgVel_%d.txt', i);
    infile = [OpenPath file];
    data(:, :, i) = csvread(infile,3,0);
end

infile2= [OpenPath 'StandardDeviations.txt'];
data2= csvread(infile2,0,0);

%find what the value of y is at (x,2)
ind=data(y,2,1);

%find the index of everytime it occurs and put all those indices in an array
indices[]
Indices=find(data(:,2,1)==ind);

%find the values for [indices,4]
for j=1:20
    for i=1:size(Indices)
        profilev(i,j)=data(Indices(i),4,j)*100;
        profileu(i,j)=data(Indices(i),3,j)*100;
        stddev(i,j)=data2(Indices(i),j);
    end
    %profile(1,j)=0;
end
numvecs=length(Indices);

sums=zeros([20 1]);
DeltD=D/numvecs;

for j=1:20
    for i=1:length(Indices)-1-x
        r1=abs(D/2-DeltD*(i-1));
        r2=r1-DeltD;
        avg=(profilev(i,j)+profilev(i+1,j))/2;
        sums(j)=(avg*(pi/2)*(r1^2-r2^2))+sums(j);
    end
end

flowrate=sums;
```

Turbulence Parameters

```
row=1118.9 %[km/m^3];
```

```

for i=1:400
    file= sprintf('PIVlab_%04d.txt', i);
    infile = [OpenPath file];
    data(:,:,i) = csvread(infile,3,0);
end

t=4 %Time Point

for i=1:10
    data_time(:,:,i)=data(:,:,20*(i-1)+t);
end

%Determine size of final plot
g=size(data_time);
g1=data(1,1,1);
indices1=find(data(:,1,1)==g1);
ind1=size(indices1); %This is the number of vectors along the wall
g2=data(1,2,1);
Indices2=find(data(:,2,1)==g2);
ind2=size(Indices2); %This is the number of vectors across the radius

%Rearrange data into contour plot format
for k=1:10
    for j=1:ind2
        for i=1:ind1
            c=i+(j-1)*ind1(1);
            u(i,j,k)=data_time(c,3,k);
            v(i,j,k)=data_time(c,4,k);
        end
    end
end

%Find u' and v'
uavg=mean(u,3);
vavg=mean(v,3);

for i=1:10
    uprime(:,:,i)=u(:,:,i)-uavg(:,:,i);
    vprime(:,:,i)=v(:,:,i)-vavg(:,:,i);
end

turbstrengthU=std(u,1,3);%Standard Deviation
turbstrengthV=std(v,1,3);%Standard Deviation

%Find u'v'
for k=1:10
    for i=1:ind1
        for j=1:ind2
            uv(i,j,k)=vprime(i,j,k).*uprime(i,j,k);
        end
    end
end

TurbIntensityU=turbstrengthU./abs(uavg);

```

```
TurbIntensityV=turbstrengthV./abs(vavg);  
rss=-row*mean(uv,3); %[Pa]
```


Appendix B- Pump Settings

Variable	Value
l1	0.02
l2	1.04
a0	4.5
a1	5.1
vs	0.8
y1	0.05
y2	0.05
k1	125
ks	26
m	10
mmin	1.3
mmax	5
th0	2
th0min	0.1
th0max	10
th1	3
th1min	0.5
th1max	10
Fc	-1
Fcmin	-5
Fcmax	10

Variable	Value
a2	1
a2min	20
a2max	1
delta	-10
deltamin	10
deltamax	250
diag1	145
diag2	65